Flight Management Systems for Hybrid-Electric Aircraft

Steven Li

A Thesis

in

The Department

of

Electrical and Computer Engineering

Presented in Partial Fulfillment of the Requirements

For the Degree of Master of Applied Science in Electrical and Computer Engineering

Concordia University

Montréal, Québec, Canada

July 2021

Concordia University

School of Graduate Studies

This is to certify that the thesis prepared

By: Steven Li

Entitled: Flight Management Systems for Hybrid-Electric Aircraft

and submitted in partial fulfillment of the requirements for the degree of

Master of Applied Science in Electrical and Computer Engineering

complies with the regulations of this University and meets the accepted standards with respect to originality and quality.

Signed by the final Examining Committee:

_____ Chair

Dr. Y. R. Shayan

_____ External Examiner

Dr. W. Lucia

_____ Examiner

Dr. K. Skonieczny

_____ Supervisor

Dr. L. Rodrigues

Approved by _____

Dr. Y. R. Shayan, Chair

Department of Electrical and Computer Engineering

_____ 2021 _____

Dr. M. Debbabi, Dean

Faculty of Engineering and Computer Science

Abstract

Flight Management Systems for Hybrid-Electric Aircraft

Steven Li

Driven by the recent development in advanced air mobility and the need to transition to more sustainable aviation, this thesis provides a framework for the optimal flight management strategy that minimizes the direct operating cost (DOC) of a hybrid-electric aircraft in steady cruise flight. Specifically, this thesis solves the minimum DOC problem for a hybrid-electric aircraft flying in a constant wind field. Polynomial equations whose positive real roots are the solutions of the minimum DOC problem are obtained using Pontryagin's minimum principle. The optimal solutions are simulated using the shooting method. The results of the shooting method are also validated using MATLAB's built-in boundary-value problem solver. Furthermore, this thesis studies the specific case of hydrogen hybrid-electric aircraft based on data found in the literature and compares it to kerosene-fuel hybrid-electric aircraft. Additionally, the optimal energy management strategy of the hybrid-electric aircraft is investigated through the simulations of multiple scenarios for two different aircraft.

Acknowledgements

Firstly, I would like to express my most sincere gratitude to my family who kept a roof over my head and my stomach well fed, and helped me go through the toughest times. To my best friend, Karen, thank you for your unconditional support which gave me strength and motivation to charge ahead. You always knew how to bring a smile to my face and to my heart.

I also wish to show my immense gratitude and acknowledge the tremendous help and support that my supervisor, Dr. Luis Rodrigues, has provided me over the past two years. His passion, guidance, and work ethics encouraged me to reach higher and to continuously improve myself. He recognized my potential and knew how to bring the best out of me. I would also like to thank Marinvent Corporation and MITACS as I am indebted to their generosity and support in funding my research.

To my good friend Clyde, thank you for being a great friend. Our discussions always left me with plenty of food for thought. To Bruno, Mitchell, Maryam, and Weihong, thank you for being the greatest colleagues I could ever ask for. The quality of your work helped elevate my own and your enthusiasm is contagious.

Last but not least, I would like to thank Concordia's faculty and staff for their continuous support during both my undergraduate and graduate studies.

Contents

List of Figures

List of Tables

Chapter 1

Introduction

1.1 Motivation

The twentieth century built the foundations for many of the technological innovations we enjoy today. One such innovation brought the world closer and changed the way we navigate our Earthly experience. This invention is the powered flight of heavier-than-air aircraft. From the first flight of the *Wright Flyer* [7] on December 17, 1903 in North Carolina to the first flight of *Ingenuity* [8] on April 19, 2021 on the planet Mars, a host of advancements in the field pushed the technology to horizons one could only dream of, a century ago. Today, aircraft fulfill a wide range of roles from the transportation of people and goods to firefighting and surveillance. They provide humanity the means to exploit a third dimension of space.

The next frontier of civil and commercial aviation is advanced air mobility (AAM). It consists of the development and expansion of air transportation systems for people and cargo in urban, local, regional, and intraregional settings [9]. Advanced air mobility will play an important role in meeting the demands of our ever more urban civilization. Over the past twenty years, humanity have experienced tremendous urban growth in cities around the world, including in Canada, as illustrated in Table 1.1. Furthermore, per the website *Our World in Data* [1], the share of the global population living in urban areas is set to exceed 60%

by the year 2030 (see Figure 1.1). Already, in 2021, more than 50% of humanity lives in urban centers. Such a rapid growth could overload the transit and transportation infrastructure. Exploiting the aerial space between and above the buildings could significantly reduce the ground traffic load and provide faster means of transportation.

Table 1.1: Population Growth in Modern Metropolitan Areas [6]

City	Country	2000	2010	2020
Montréal	Canada	3,428,971	3,896,932	4,220,566
Toronto	Canada	4,607,142	5,499,233	6,196,731
Vancouver	Canada	1,959,037	2,278,216	2,581,079
Tokyo	Japan	34,449,908	36,859,626	37,393,128
Delhi	India	15,691,899	21,987,896	30,290,936
Shanghai	China	14,246,541	20,314,308	27,058,480
São Paulo	Brazil	17,014,078	19,659,808	22,043,028

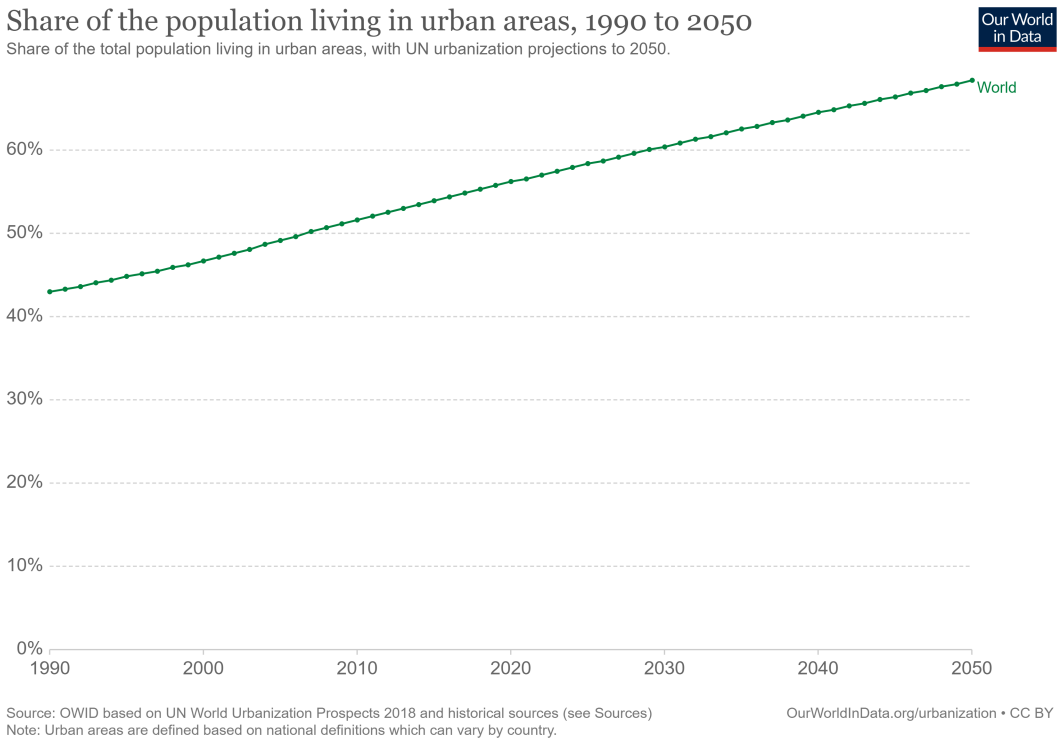

Figure 1.1: Urbanization of the World population [1]

Although AAM is a promising solution to the urbanization problem, it brings challenges of its own. One such challenge is its sustainability. Currently, the great majority of aircraft

in service rely on combustible fuels such as diesel and kerosene to fly. However, such fuels are non-renewable and their combustion produces greenhouse gases (GHGs) which are the leading causes of our current climate crisis. One way to mitigate this issue is to use sustainable fuels such as bio-fuels. A major advocate for this solution is the aircraft manufacturer Boeing [10]. Bio-fuels do not require significant changes to the existing infrastructure and are compatible with current technologies [11]. However, bio-fuels are still hydrocarbon fuels and their combustion produces greenhouse gases.

Another solution is hydrogen fuel and is supported by aircraft manufacturers such as Airbus [12]. Hydrogen aircraft do not emit GHGs. They only produce heat and water. Their performance is on par with conventional aircraft [13]. However, the development of this technology is still in its infancy and may require many years, or even decades, to become a viable technology.

A third path to achieve sustainable aviation is all-electric aircraft. Such aircraft do not directly emit any greenhouse gases and the technology for electric propulsion currently exists. However, battery technologies are a crucial limiting factor in the widespread use of all-electric aircraft. Larger, longer-range all-electric aircraft are not yet a viable option to replace conventional aircraft [14]. Furthermore, charging the batteries in the electric grid may overload the current grid. Therefore, hybrid-electric aircraft may be a better solution to the sustainability problem, for the moment. Hybrid-electric aircraft use fuel energy and electrical energy for propulsion. The fuel can be hydrogen, a bio-fuel, or a conventional fuel. The benefits include a reduction in emissions of GHGs and the use of existing technologies [15][16]. As the technology for all-electric propulsion improves, the hybrid-electric aircraft will be able to reduce its carbon footprint.

Another challenge faced by AAM is autonomous guidance and navigation. The airspace in AAM will be composed of both manned and unmanned aircraft. In such a complex environment, human pilots may become obsolete and the aircraft will be required to fly autonomously. The aircraft will need to be able to avoid collisions with static obstacles

such as buildings and dynamic obstacles such as birds and other vehicles. Furthermore, to reduce the energy consumption of the aircraft, to travel faster between destinations, and to prioritize certain vehicles such as aerial emergency vehicles, the aircraft system will need to have the ability to plan either a priori, or in real-time, optimal trajectories and follow such trajectories. These trajectories must also guarantee the safety of the aircraft and of the people in and around it. An additional challenge related to that of autonomous guidance and navigation is that of urban air traffic management (UTM). A denser and more complex airspace will require robust and safe air traffic management systems. Current air control may not have the ability to keep up with the amount of air traffic expected with AAM where both manned and unmanned vehicles share a common airspace. The challenges of UTM also include urban air quality, prioritizing emergency vehicles, and use of both air and ground capabilities when possible.

With a denser airspace and more aircraft in service, a challenge arises regarding the refueling, recharging, and service infrastructure for AAM. Existing infrastructure may not be enough to sustain the air traffic which will come with AAM. The rise of AAM implies more air traffic between cities which would require more airports or more efficient airports. It also implies more urban air traffic, likely to be mostly composed of vertical take-off and landing (VTOL) aircraft [17], which will require urban take-off and landing platforms.

Finally, safety must remain the main priority while developing AAM. The risk to human life and property damage must be minimized for AAM to be safe and viable. To guarantee the safety of AAM, laws and regulations must be set in place and safety must be the highest priority in designing, testing, and manufacturing AAM systems.

1.2 Literature Survey

1.2.1 Advanced Air Mobility

The earliest mention of Advanced Air Mobility (AAM) in the literature, to the best of our knowledge, occurred in the 1970s and referred to the rapid deployment of military aerial capabilities [18][19]. However, AAM in a civil aviation context is a relatively new idea coined by NASA in 2019 to describe the development of aerial capabilities for civil transportation in regional, urban and suburban settings [9]. Since then, many researchers are building frameworks to guide the research and development of AAM. For instance, Wing et al. proposed an approach to develop the technologies for AAM using simplified vehicle dynamics [20]. Chancey et al. suggested a framework for better cooperation between humans and machines known as human-autonomy teaming [21][22]. Furthermore, researchers are exploring avenues to create safe air traffic management (ATM) systems for AAM such as decentralized ATM [23].

A subset of AAM is Urban Air Mobility (UAM) which focuses on air mobility in urban settings specifically. There are multiple facets to UAM. Among them are urban air traffic management (UTM), service infrastructures, aircraft flight and energy management, and safety.

For urban air traffic management, the majority of studies were performed recently. Lundberg et al. investigated sample side-effects of unmanned traffic management systems and suggested using advanced dynamic airspace components to address effects of UTM interventions [24]. For the implementation of UTM, first-come-first-serve [25] and reservation of airspace [26] approaches have been proposed. Furthermore, UTM may present with a scheduling problem which is studied by Kim et al. In that paper, a formulation of the scheduling problem for urban mobility is proposed based on particle swarm optimization and a genetic algorithm. Its objective is to maximize net profit and minimize final queue size.

In planning the optimal flight path for an aircraft, one must consider the optimization objective. For example, one may consider minimizing operating costs or energy consumption. Li et al. proposed a hybrid optimization method to reconfigure UAV formations with collision and communication constraints in three-dimensional space [27]. Furthermore, Kim et al. proposed an optimal path planning algorithm using the Hermite-Simpson collocation method based on the energy consumption of a solar-powered UAV while accounting for wind fields. Their optimization objectives were to maximize input energy and minimize output energy [28]. Then, He et al. suggested an optimal solution for the waypoint-following guidance law problem with linear autopilot dynamics to minimize the energy consumption of the aircraft [29]. Similarly, De Paiva et al. considered the optimal trade-off guidance between time and energy costs with time-varying wind fields. They based their problem formulation on the zero-effort-miss/zero-effort-velocity approach where gravity is replaced by wind acceleration. In addition, with UAM, the airspace is bound to become denser, therefore robust conflict resolution algorithm must be developed. One such algorithm aims to minimize the deviation from the original flight path using an heuristic method. This approach suggests that the aircraft may enter the airspace without a fixed prior flight plan [30]. Another approach is to compute and correct intersecting trajectories by formulating the problem as a mixed integer linear program and by using a learning-based approach [31].

1.2.2 Hybrid-Electric Aircraft

A major obstacle in the development of AAM is its sustainability. As the effects of climate change grow in intensity and frequency, the international community came together and committed itself to combat this threat. Multiple international and national bodies have set goals and legislated regulations to reach sustainability and to reduce GHG emissions. Notably, the International Civil Aviation Organization (ICAO) established, in 2010, a set of objectives to improve fuel efficiency and reduce carbon emissions [32]. Additionally, they adopted Resolution A40-18 to consolidate policies and practices in civil aviation to diminish its impact

on climate change. One course of action undertaken by the aerospace industry to address this crisis is to develop hybrid-electric and all-electric aircraft. In fact, ICAO compiled a list of 32 all-electric and 7 hybrid-electric aircraft projects [33] with notable examples of these development efforts including Airbus' E-Fan X[1], Boeing's SUGAR Volt, Faradair's Bio Electric Hybrid Aircraft, and the EAG Hybrid Electric Regional Aircraft. The main drawback of all-electric aircraft is the energy density of batteries. Current battery technologies have limited mass specific energy, which restricts the size of the batteries an aircraft can carry. Consequently, all-electric aircraft will most likely be constrained to regional and recreational flying. In contrast, hybrid-electric aircraft can reduce fuel consumption significantly while being a serious challenger to large commercial jets.

Early work on hybrid-electric aircraft focused on the feasibility of incorporating electrical energy into aircraft propulsion systems [34][35][36][37]. The findings concluded that hybrid-electric aircraft can significantly reduce fuel consumption while maintaining the endurance of conventional aircraft. In the mid-2000s, researchers started to investigate different control strategies to reduce fuel consumption in hybrid-electric unmanned aerial vehicles (UAVs) through neural networks [38] and rule-based controllers [39]. Following ICAO's goals statement in 2010, research and development of hybrid-electric aircraft grew drastically. Most of the studies that emerged in the first half of the 2010s focused on the design of hybrid-electric aircraft. Pornet et al. [40] developed an expression to evaluate the cost specific air range (COSAR) of a hybrid-electric aircraft based on energy cost. They also derived a cost index defined as a trade-off between time-related costs and energy costs and demonstrated the application of the COSAR and the cost index by minimizing the operating costs of the aircraft. The later half of the 2010s saw a rise in the optimal control research of hybrid-electric aircraft. In 2016, Falck and Gray [41] tackled the trajectory optimization problem for hybrid-electric aircraft using an implicit Legendre-Gauss-Lobatto collocation method with adjoint derivatives. In the following year, Bongermino et al. [42] used dynamic program-

[1]Unfortunately, the E-Fan X collaborative development between Airbus, Siemens, and Rolls-Royce has been discontinued in April 2020

ming to find an optimal power management strategy for hybrid-electric aircraft. In the same year, Donateo and Spedicato [43] investigated the endurance of hybrid-electric aircraft by developing an on-off energy management strategy. In 2018, multiple papers on the optimal control of hybrid-electric aircraft were published. Boggero et al. [44] proposed the use of fuzzy logic to minimize fuel and maximum takeoff weight at a preliminary design level. Donateo et al. [45] used a genetic algorithm to optimize the operating points of the aircraft engine with the end goal of minimizing fuel consumption. Geiss et al. [46] employed the `fmincon` function in MATLAB to minimize fuel consumption and operating costs. They defined the operating cost function based on fuel and electricity costs as well as on battery and internal combustion engine depreciation costs. In 2020, Doff-Sotta et al. [47] published a paper where they proposed an energy management strategy of hybrid-electric aircraft based on model predictive control coupled with convex optimization. Similarly, Leite and Voskuijl [48] suggested an energy management strategy based on dynamic programming. Wall and Meyer also proposed an optimal power management strategy using model predictive control [49] and Wang and Koein provided a solution for an optimal energy management strategy based on hierarchical model predictive control [50]. In addition, de Vries et al. derived a range equation for conventional, all-electric and constant power-split hybrid-electric aircraft [51]. Moreover, some authors explored the optimal control of airships. One paper proposed an energy management strategy for solar powered hybrid-energy airships. The strategy involves splitting the energy from the photovoltaic cells to the load and the energy storage devices [52]. Airships could be a sustainable means of transportation for commutes where the passengers do not mind longer duration flights to arrive at a given destination. In the first half of 2021, Hashemi et al. developed a lithium-ion battery model using machine learning which could be used in all-electric and hybrid-electric battery management systems [53]. Additionally, Wang and Mesbahi found an optimal power management of a hybrid-electric aircraft in climb, cruise and descent to minimize fuel consumption where the aircraft engines need to operate in their higher efficiency regions [54]. Furthermore, Lee et al. proposed a

method that combines the optimal power split and flight path trajectories to minimize fuel consumption using differential dynamic programming [55].

Although solutions to the Direct Operating Cost (DOC) minimization problem for fuel-based and all-electric aircraft are provided by [5] and [3], respectively, to the best of our knowledge, only the work in references [40] and [46] sought to minimize the operating cost of hybrid-electric aircraft. In the study performed by Pornet et al. [40], the authors defined a cost function in a similar manner as the cost function presented in Chapter 3. However, the authors assumed a constant velocity to solve the optimization problem. In the work carried out by Geiss et al. [46], the authors defined the operating cost based on fuel, electricity and depreciation costs with the power generated, the velocity of the aircraft and the duty cycle of the battery as optimization parameters. Furthermore, the authors assumed a constant velocity and a constant power generated. In contrast, this thesis addresses the minimization of the direct operating cost for a hybrid-electric aircraft in one-dimensional and two-dimensional space with a time-varying velocity. Furthermore, for the one-dimensional case, the DOC optimal control problem is solved for an aircraft in a constant wind field. A case study of hydrogen hybrid-electric aircraft is also provided. Additionally, this thesis proposes an optimal energy management strategy based on the proportion of the thrust coming from electrical energy.

In summary, from the literature survey of hybrid-electric aircraft, it seems that there are still gaps regarding the optimal direct operating cost problem. Only two papers addressed this problem and both were published in the past decade. This thesis provides a framework for the optimal flight management strategy that minimizes the direct operating cost (DOC) of a hybrid-electric aircraft in steady cruise flight.

1.2.3 Hydrogen Aircraft

With the growing interests towards sustainable fuels, many in the aviation industry are turning to liquid hydrogen as the replacement for conventional fuels. Some of the first

studies on the viability of hydrogen as an aircraft fuel were performed in the 1960s and 1970s where hydrogen was suggested as a fuel for supersonic flight [56] and as an alternative to jet fuel [57][58].

The environmental benefits of hydrogen fuel became more apparent as reports of Earth warming emerged. In a study published in 1990, the author detailed how liquid hydrogen could help reduce greenhouse gases emissions [59]. Then, in 1997, Contreras et al. compared the benefits of hydrogen fuel to conventional fuels [60]. In the 2000s, a few papers studied the challenges of hydrogen aircraft and pushed the concept further. Notably. Sefain discussed hydrogen aircraft concepts and their required ground support [61]. Furthermore, multiple researchers published papers on the development of CRYOPLANE, an European initiative to study the feasibility of hydrogen aircraft. Their conclusions were that hydrogen fuel provided mass savings, cooler engines, but a difficult developmental challenge from kerosene-based technologies [62][63][64]. Then, Maniaci studied the performance of hydrogen aircraft compared to conventional aircraft and concluded that hydrogen aircraft have the potential to drastically decrease the direct operating cost [65].

A few studies in recent years have studied the fuel consumption model of hydrogen aircraft. Notably, Corchero et al. [63], Amy et. al [66], Derakhshandeh et al. [67], and Boggia et al. [68] developed fuel consumption models and provided data on the thrust specific fuel consumption as well as other parameters of different turbofan engines. However, to the best of our knowledge, there is no comparative study of the thrust specific fuel consumption for multiple hydrogen-fuel and kerosene-fuel turbofan engines as provided in this thesis.

1.3 Contributions

This thesis addresses three problems of optimal flight management and energy management of hybrid-electric aircraft based on the direct operating cost of the aircraft. The contributions in this work are detailed below.

1. In Chapter 3, the first problem addressed is the minimization of the Direct Operating Cost (DOC) of a hybrid-electric aircraft without wind considering only the longitudinal flight dynamics. To solve this problem, an energy management parameter, called the hybridization coefficient in this thesis, is defined as the proportion of the total thrust of the hybrid-electric aircraft which comes from electrical energy. A quintic polynomial whose positive real roots are solutions to the minimum DOC problem is then found using Pontryagin's Minimum Principle (PMP). Furthermore, a case study of hydrogen hybrid-electric aircraft is performed and compared to the literature and to the solutions developed in Chapter 3. Additionally, the optimal energy management strategy of a hybrid-electric aircraft is investigated and suggested based on the hybridization coefficient.

2. In Chapter 4, the second problem extends the first problem to account for constant wind. A sextic polynomial whose positive real roots are solutions of the minimum DOC problem is found using PMP. Then, the effects of wind speed on the optimal cruise airspeed, the energy consumption, and the direct operating cost are investigated. Finally, the third problem is an extension of the first problem to the steady cruise flight in the horizontal plane and defined for a weak wind and constant heading scenario. A quintic polynomial whose positive real roots are solutions to this problem is obtained using PMP with simulations supporting the solutions.

1.4 Thesis Structure

This thesis will be subdivided into the following chapters. First, Chapter 2 provides an overview of theoretical preliminaries required in this thesis. These preliminaries include concepts in aerodynamics, the propulsion model for hybrid-electric and hydrogen aircraft, a review of optimal control and the Pontryagin Minimum Principle (PMP), Descartes' rule of signs, and the shooting method. s Chapter 3 then finds the optimal airspeed using PMP

that minimizes the Direct Operating Cost (DOC) of a hybrid-electric aircraft in steady cruise flight without wind using its longitudinal flight dynamics. An optimal energy management strategy is suggested. A case of study of hydrogen hybrid-electric aircraft is subsequently performed.

Finally, in Chapter 4, the optimal DOC problem is extended to steady cruise flight subject to constant wind speeds. The effects of wind speed on the optimal cruise airspeed, the energy consumption, and on the DOC are investigated. Then, the optimal DOC problem is extended to steady cruise flight in the horizontal plane and a solution is found using the Pontryagin minimum principle.

Chapter 2

Theoretical Preliminaries

2.1 Introduction

In this chapter, a review of theoretical preliminaries for this thesis is performed. In Section 2.2, concepts in aerodynamics are reviewed including aerodynamic forces, flight attitude, and flight dynamics. Then, the propulsion models for hybrid-electric and hydrogen aircraft are presented in Section 2.3. Subsequently, in Section 2.4, a brief review of optimal control and the Pontryagin's minimum principle is carried out. This is followed by a review of Descartes' rule of signs in Section 2.5. Finally, the shooting method is explained in Section 2.6.

2.2 Concepts in Aerodynamics

The powered flight of hybrid-electric aircraft requires a thorough understanding of the forces acting on the aircraft, the flight attitude, and the flight dynamics of the aircraft. Each of these concepts will be reviewed in this section.

2.2.1 Aerodynamic Forces

An aircraft in flight is subject to the thrust produced by its propulsion system, its weight which depends on the aircraft's mass and the local gravitational field, and the aerodynamic

forces. The resultant force exerted on the aircraft is

$$\boldsymbol{F} = \boldsymbol{T} + \boldsymbol{F_A} + \boldsymbol{W} \tag{2.1}$$

where $\boldsymbol{F}$ is the resultant force, $\boldsymbol{T}$ is the thrust force, $\boldsymbol{F_A}$ is the aerodynamic force, and $\boldsymbol{W}$ is the weight force. The aerodynamic force can be separated into a component parallel to the direction of the air flow and a component perpendicular to the direction of the air flow as

$$\boldsymbol{F_A} = \boldsymbol{D} + \boldsymbol{L} \tag{2.2}$$

where $\boldsymbol{D}$ is the drag force and $\boldsymbol{L}$ is the lift force. In the case of an aircraft in flight, the direction of the air flow is the direction of the velocity of the aircraft. The component parallel to the velocity is the drag force and the component perpendicular to the velocity is the lift force.

The lift $\boldsymbol{L}$ and drag $\boldsymbol{D}$ forces are given respectively by [69]

$$\boldsymbol{L} = \frac{1}{2}\rho S \boldsymbol{v}^2 C_L \tag{2.3}$$

$$\boldsymbol{D} = \frac{1}{2}\rho S \boldsymbol{v}^2 C_D \tag{2.4}$$

where $\boldsymbol{v}$ is the airspeed, ρ is the altitude-dependent air density, S is the wing surface area, and C_L and C_D are the lift and drag coefficients, respectively.

If the aircraft is in steady flight, is below the drag divergence Mach number, and follows a drag polar curve, one can derive the equations for the coefficients of lift and drag, given that $\rho S v^2 \neq 0$, as [69]

$$C_L = \frac{2W}{\rho S v^2} \tag{2.5}$$

$$C_D = C_{D,0} + C_{D,2}\left(\frac{2W}{\rho S v^2}\right)^2 \tag{2.6}$$

where $C_{D,0}$ is the zero-lift drag coefficient and $C_{D,2}$ is the induced drag coefficient. Hence, the drag force in (2.4) can be rewritten as

$$D = D(v, W) = \frac{1}{2} C_{D,0} \rho S v^2 + \frac{2 C_{D,2} W^2}{\rho S v^2} \tag{2.7}$$

2.2.2 Flight Attitude

The flight attitude of an aircraft describes its angular position in space during flight. An aircraft flying in three-dimensional space is subject to six degrees of freedom, namely longitudinal, lateral, and vertical displacement and pitch, roll, and yaw rotations. Figures 2.1 and 2.2 describe visually the flight attitude of the aircraft.

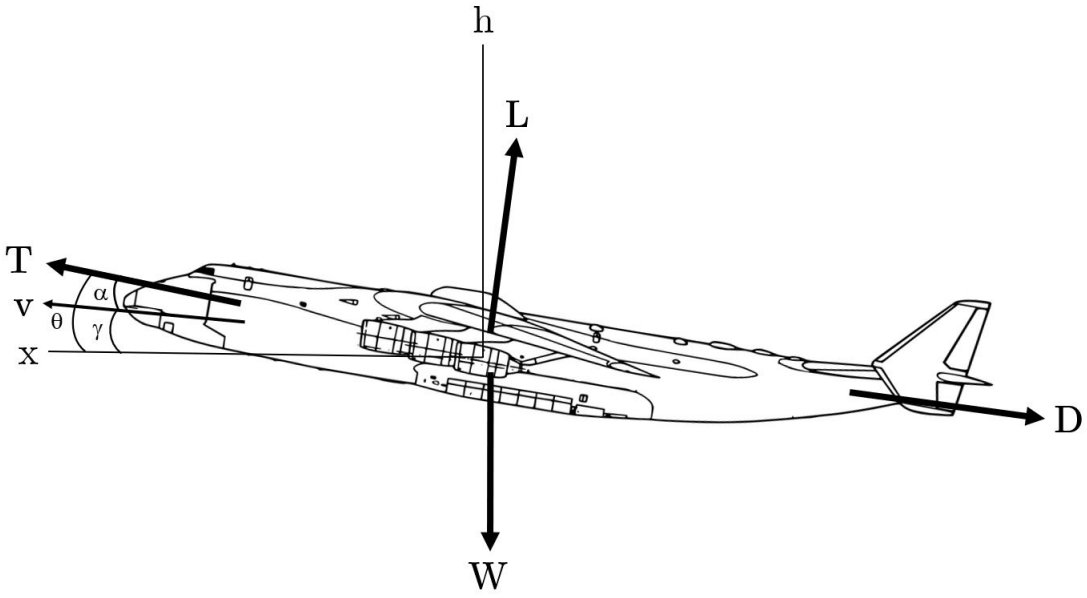

Figure 2.1: Longitudinal flight attitude (adapted from [2])

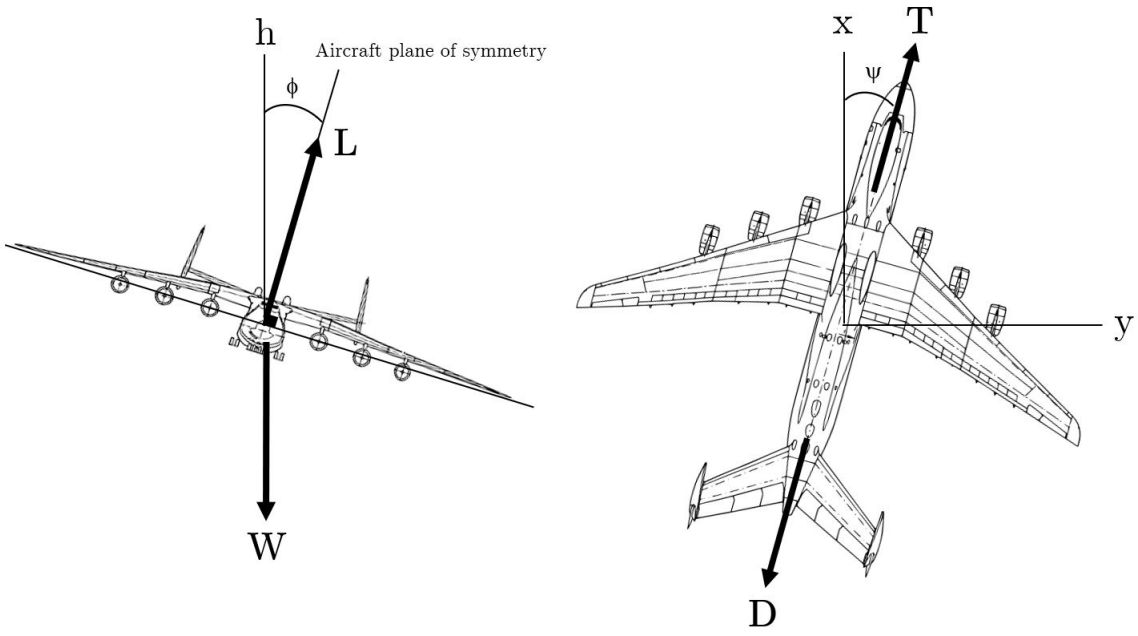

Figure 2.2: Lateral flight attitude (adapted from [2])

In Figures 2.1 and 2.2, $\boldsymbol{v}$ is the velocity of the aircraft relative to the air mass, x, y, and h are the latitudinal, the longitudinal, and the vertical axis of the Earth-centered inertial frame of reference, respectively, α is the angle of attack, γ is the flight path angle, ϕ is the bank angle, ψ is the heading angle, and θ is the pitch angle.

Two frames of references are commonly used to describe the orientation of an aircraft in flight, namely the aircraft body frame B and the Earth-centered inertial frame I. To transform the aircraft attitude from the inertial frame to the body frame, one must consider the yaw, pitch, and roll rotations consecutively [70].

First, the rotation matrix for yaw transforms the orientation of the aircraft from the inertial frame to a vehicle frame V_1 and is described by

$$R_I^{V_1}(\psi) = \begin{bmatrix} \cos\psi & \sin\psi & 0 \\ -\sin\psi & \cos\psi & 0 \\ 0 & 0 & 1 \end{bmatrix} \tag{2.8}$$

Then, the rotation matrix for pitch, given $\theta = \alpha + \gamma$, transforms the orientation of the

aircraft from the vehicle frame V_1 to a second vehicle frame V_2 and is described by

$$R_{V_1}^{V_2}(\theta) = \begin{bmatrix} \cos\theta & 0 & -\sin\theta \\ 0 & 1 & 0 \\ \sin\theta & 0 & \cos\theta \end{bmatrix} \tag{2.9}$$

Finally, the rotation matrix for roll transforms the orientation of the aircraft from the second vehicle frame V_2 to the body frame B and is described by

$$R_{V_2}^{B}(\phi) = \begin{bmatrix} 1 & 0 & 0 \\ 0 & \cos\phi & \sin\phi \\ 0 & -\sin\phi & \cos\phi \end{bmatrix} \tag{2.10}$$

Combining the rotation matrices for roll, pitch, and yaw yields the transformation of the orientation of the aircraft from the body frame to the inertial frame and is obtained as the product of (2.10), (2.9), and (2.8) as [70]

$$R_I^B(\phi,\theta,\pi) = R_{V2}^B(\phi)R_{V1}^{V2}(\theta)R_I^{V1}(\psi) = \begin{bmatrix} \cos\theta\cos\psi & \cos\theta\sin\psi & -\sin\theta \\ \sin\phi\sin\theta\cos\psi - \cos\phi\sin\psi & \sin\phi\sin\theta\sin\psi + \cos\phi\cos\psi & \sin\phi\cos\theta \\ \cos\phi\sin\theta\cos\psi + \sin\phi\sin\psi & \cos\phi\sin\theta\sin\psi - \sin\phi\sin\psi & \cos\phi\cos\theta \end{bmatrix} \tag{2.11}$$

2.2.3 Flight Dynamics

The three-dimensional dynamic model of an aircraft in symmetric flight subject to constant wind can be expressed as a set of nonlinear ordinary differential equations [71][72] as

$$\dot{x} = v\cos\gamma\cos\psi + v_{w,x} \tag{2.12}$$

$$\dot{y} = v\cos\gamma\sin\psi + v_{w,y} \tag{2.13}$$

$$\dot{h} = v \sin\gamma + v_{w,h} \tag{2.14}$$

$$\dot{v} = \left(\frac{g}{W}\right)(T\cos\alpha - D - W\sin\gamma) \tag{2.15}$$

$$\dot{\psi} = \left(\frac{g}{Wv\cos\gamma}\right)(T\sin\alpha + L)\sin\phi \tag{2.16}$$

$$\dot{\gamma} = \left(\frac{g}{Wv}\right)((T\sin\alpha + L)\cos\phi - W\cos\gamma) \tag{2.17}$$

$$\dot{\phi} = \left(\frac{g}{Wv}\right)(T\sin\alpha + L)\cos\phi\tan\gamma \tag{2.18}$$

$$\dot{W} = -S_{fc}T \tag{2.19}$$

where x is the latitudinal position, y is the longitudinal position, h is the altitude, v is the airspeed, ψ is the heading angle, γ is the flight path angle, W is the weight, α is the angle of attack, ϕ is the bank angle, $v_{w,x}$, $v_{w,y}$, and $v_{w,h}$ are the longitudinal, lateral, and vertical wind speeds, respectively, g is the gravitational acceleration, T is the magnitude of the total thrust force, D is the magnitude of the drag force, L is the magnitude of the lift force, and S_{fc} is the thrust specific fuel consumption.

2.2.3.1 Longitudinal Flight Dynamics

In the dynamics of (2.12)-(2.19), consider a constant heading angle ψ of 0, a bank angle ϕ of 0, and a constant latitudinal position y (i.e. $\dot{\psi} = \psi = \phi = \dot{y} = 0$). Then one gets the equations of the aircraft in the vertical plane as

$$\dot{x} = v\cos\gamma + v_{w,x} \tag{2.20}$$

$$\dot{h} = v\sin\gamma + v_{w,h} \tag{2.21}$$

$$\dot{v} = \left(\frac{g}{W}\right)(T\cos\alpha - D - W\sin\gamma) \tag{2.22}$$

$$\dot{\gamma} = \left(\frac{g}{Wv}\right)(T\sin\alpha + L - W\cos\gamma) \tag{2.23}$$

$$\dot{W} = -S_{fc}T \tag{2.24}$$

If the altitude remains constant (i.e. $\dot{h} = \dot{\gamma} = \gamma = 0$) and the thrust perpendicular to the velocity is small compared to weight and lift, one gets the longitudinal flight dynamics along the aircraft's body frame

$$\dot{x} = v + v_{w,x} \tag{2.25}$$

$$\dot{v} = \left(\frac{g}{W}\right)(T\cos\alpha - D) \tag{2.26}$$

$$\dot{W} = -S_{fc}T \tag{2.27}$$

$$L = W \tag{2.28}$$

2.2.3.2 Dynamics in the Horizontal Plane

Considering the dynamics of (2.12)-(2.19), if the altitude remains constant (i.e. $\dot{h} = \dot{\gamma} = \gamma = 0$) and the thrust perpendicular to the velocity is small compared to weight and lift, then the dynamics in the horizontal plane are

$$\dot{x} = v\cos\psi + v_{w,x} \tag{2.29}$$

$$\dot{y} = v\sin\psi + v_{w,y} \tag{2.30}$$

$$\dot{v} = \left(\frac{g}{W}\right)(T\cos\alpha - D) \tag{2.31}$$

$$\dot{\psi} = \left(\frac{g}{Wv}\right)(T\sin\alpha + L)\sin\phi \tag{2.32}$$

$$\dot{W} = -S_{fc}T \tag{2.33}$$

$$L\cos\phi = W \tag{2.34}$$

2.3 Propulsion Model

2.3.1 Hybrid-Electric Propulsion

The propulsion system of hybrid-electric aircraft uses two different energy sources to generate the aircraft thrust. One of the energy sources stems from a fuel which can be, but is not limited to, kerosene, diesel, or liquid hydrogen, and the other is electricity which can come from batteries, solar cells, or fuel cells. The fuel consumption of the hybrid-electric aircraft may be expressed as

$$\dot{W} = -S_{fc}T_{jet} \tag{2.35}$$

where T_{jet} is the thrust generated by the jet engines and is defined as

$$T_{jet} = (1 - \beta)T \tag{2.36}$$

where $\beta \in [0, 1]$ is the hybridization coefficient and describes the level of hybridization of the aircraft as the proportion of the thrust coming from electrical energy. For example, if $\beta = 0.8$, then 80% of the thrust comes from electrical energy and 20% comes from fuel energy. If $\beta = 1$, the thrust of the aircraft comes strictly from electrical energy. In contrast, if $\beta = 0$, the energy propelling the aircraft is generated strictly by the combustion of fuel.

To determine the rate of electricity consumption, one considers the total power P_{tot} required by the aircraft which is the sum of the power delivered by the jet engine P_{jet} and the available battery power P_e (after losses caused by the conversion of electrical to mechanical energy) and is defined as

$$P_{tot} = Tv = P_{jet} + \eta P_e = (1 - \beta)Tv + \beta Tv \tag{2.37}$$

where η is the electrical to mechanical energy conversion efficiency. The battery output

power is given by

$$P_e = Ui = -U\dot{Q} \tag{2.38}$$

where Q is the electric charge stored in the battery, U is the battery output voltage, and i is the battery output current. Based on (2.37) and (2.38), one can derive the expression for the flow of electric charge as

$$\dot{Q} = -\frac{\beta T v}{\eta U} \tag{2.39}$$

The total energy consumption of the system is a linear combination of the fuel consumption and of the electricity consumption.

2.3.2 Liquid Hydrogen Fuel

The fuel consumption model based on the combustion of liquid hydrogen is the same as that for conventional fuels [73]. The main difference lies in the thrust specific fuel consumption.

The combustion process of hydrogen is as follows [74]

$$2H_2 + O_2 \rightarrow 2H_2O + heat \tag{2.40}$$

In comparison, the combustion process of a hydrocarbon fuel such as kerosene can be approximated by [75]

$$C_{12}H_{24} + 18O_2 \rightarrow 12CO_2 + 12H_2O + heat \tag{2.41}$$

Comparing the combustion process of hydrogen to that of conventional hydrocarbon fuels, one can observe that one of the main advantages of hydrogen combustion is the lack of carbon dioxide, a potent greenhouse gas, as a combustion product.

2.4 Optimal Control

To find the optimal flight management strategy of a hybrid-electric aircraft, one requires optimal control theory. Optimal control problems are solved using two main methods. The first method is dynamic programming which is based on Bellman's principle of optimality [76]. The second method is Pontryagin's minimum principle (PMP) [77] which can be derived from calculus of variations when one assumes differentiability. The optimal control problems in this thesis will be solved using the minimum principle. This section will provide an overview of this principle.

2.4.1 Optimal Control Problem Formulation

The objective of optimal control is to find a control input $\boldsymbol{u} \in \mathbb{R}^m$ where $m \in \mathbb{N}^+$ for a dynamic system with states $\boldsymbol{x} \in \mathbb{R}^n$ where $n \in \mathbb{N}^+$, which optimizes an objective or a cost functional J from a known initial state to a desired final state.

If the function $L(t, \boldsymbol{x}(t), \boldsymbol{u}(t))$ is integrable, a free final time optimal control problem can be formulated as

$$\begin{aligned} J^* = &\min_{\boldsymbol{u}, t_f} \left[\phi(t_f, \boldsymbol{x}(t_f)) + \int_{t_0}^{t_f} L(t, \boldsymbol{x}(t), \boldsymbol{u}(t)) dt \right] \\ &\textit{subject to} \\ &\dot{\boldsymbol{x}}(t) = f(\boldsymbol{x}(t), \boldsymbol{u}(t)) \\ &t \in [t_0, t_f] \\ &\boldsymbol{\Psi}(\boldsymbol{x}(t_0), \boldsymbol{x}(t_f)) = \boldsymbol{0} \end{aligned} \tag{2.42}$$

which is known as the Bolza formulation where $\boldsymbol{\Psi}$ is the vector of initial and terminal constraints defined in this thesis as

$$\boldsymbol{\Psi}(\boldsymbol{x}(t_0), \boldsymbol{x}(t_f)) = \begin{bmatrix} \boldsymbol{x}(t_0) - \boldsymbol{x}_0 \\ \boldsymbol{x}(t_f) - \boldsymbol{x}_f \end{bmatrix} \tag{2.43}$$

2.4.2 Optimality Conditions

To use the Pontryagin's minimum principle, one needs to formulate the Hamiltonian

$$H(t, \boldsymbol{x}(t), \boldsymbol{u}(t), \boldsymbol{J_x}(t)) = L(t, \boldsymbol{x}(t), \boldsymbol{u}(t)) + \boldsymbol{J_x}^T \cdot f(\boldsymbol{x}(t), \boldsymbol{u}(t)) \tag{2.44}$$

where $\boldsymbol{J_x}$ is known as the co-state vector and is defined as the partial derivative of the optimal cost-to-go with respect to the states. Let

$$\boldsymbol{\Phi}(t_f, \boldsymbol{x}(t_f)) = \phi(t_f, \boldsymbol{x}(t_f)) + \boldsymbol{\nu}^T \boldsymbol{\Psi}(\boldsymbol{x}(t_0), \boldsymbol{x}(t_f)) \tag{2.45}$$

where $\boldsymbol{\nu}$ is a Lagrange multiplier.

Theorem 1 (Pontryagin's Minimum Principle [78])**.** *If $\boldsymbol{x}^*(t)$, $\boldsymbol{J}^*_{\boldsymbol{x}}(t)$, and $\boldsymbol{u}^*(t)$ are the optimal states, co-states, and control inputs of the optimal control problem (2.42) $\forall t \in [t_0, t_f^*]$ where t_f^* is the optimal free final time and $\boldsymbol{x}(t)$, $\boldsymbol{u}(t)$, $L(t, \boldsymbol{x}(t), \boldsymbol{u}(t))$, $H(t, \boldsymbol{x}^*(t), \boldsymbol{u}^*(t), \boldsymbol{J}^*_{\boldsymbol{x}}(t))$, and $\boldsymbol{\Psi}(\boldsymbol{x}(t_0), \boldsymbol{x}(t_f))$ are all class C^1 functions, then*

1. $H(t, \boldsymbol{x}^*(t), \boldsymbol{u}^*(t), \boldsymbol{J}^*_{\boldsymbol{x}}(t)) \leq H(t, \boldsymbol{x}^*(t), u, \boldsymbol{J}^*_{\boldsymbol{x}}(t)),\ \forall \boldsymbol{u} \in \mathbb{R}^m, \forall t \in [t_0, t_f^*]$.
2. $\dot{\boldsymbol{J}}^*_{\boldsymbol{x}}(t) = -\nabla_{\boldsymbol{x}} H(t, \boldsymbol{x}^*(t), \boldsymbol{u}^*(t), \boldsymbol{J}^*_{\boldsymbol{x}}(t)),\ \forall t \in [t_0, t_f^*]$.
3. $\boldsymbol{J}^*_{\boldsymbol{x}}(t_f^*) = \nabla_{\boldsymbol{x}} \boldsymbol{\Phi}(t_f^*, \boldsymbol{x}^*(t_f^*))$.
4. $\dot{\boldsymbol{x}}(t) = \nabla_{\boldsymbol{J_x}} H(t, \boldsymbol{x}^*(t), \boldsymbol{u}^*(t), \boldsymbol{J}^*_{\boldsymbol{x}}(t)),\ \forall t \in [t_0, t_f^*]$.
5. $H(t_f^*, \boldsymbol{x}^*(t_f^*), \boldsymbol{u}^*(t_f^*), \boldsymbol{J}^*_{\boldsymbol{x}}(t_f^*)) + \frac{\partial \boldsymbol{\Phi}(t_f^*, \boldsymbol{x}^*(t_f^*))}{\partial t_f^*} = 0$.

Proof. A proof of this theorem is provided in [77]. □

If the Hamiltonian (2.44) is a class C^1 function, then the first-order necessary condition of optimality with respect to the control $\boldsymbol{u}(t)$ for a free final time t_f^* is

$$\nabla_{\boldsymbol{u}} H(t, \boldsymbol{x}(t), \boldsymbol{u}(t), \boldsymbol{J_x}(t)) = \boldsymbol{0},\ \forall t \in [t_0, t_f^*] \tag{2.46}$$

Additionally, if the Hamiltonian (2.44) is a class C^2 function, then the second-order necessary condition for a minimum with respect to the control $\boldsymbol{u}(t)$ is

$$\nabla^2_{\boldsymbol{uu}} H(t, \boldsymbol{x}(t), \boldsymbol{u}(t), \boldsymbol{J_x}(t)) \geq \boldsymbol{0},\ \forall t \in [t_0, t_f^*] \tag{2.47}$$

The time derivative of the Hamiltonian is defined, using the multivariate chain rule, as

$$\begin{aligned} \dot{H}(t, \boldsymbol{x}^*(t), \boldsymbol{u}^*(t), \boldsymbol{J}^*_{\boldsymbol{x}}(t)) &= \frac{\partial H(t, \boldsymbol{x}^*(t), \boldsymbol{u}^*(t), \boldsymbol{J}^*_{\boldsymbol{x}}(t))}{\partial t} + \nabla_{\boldsymbol{x}} H(t, \boldsymbol{x}^*(t), \boldsymbol{u}^*(t), \boldsymbol{J}^*_{\boldsymbol{x}}(t)) \dot{\boldsymbol{x}} \\ &+ \nabla_{\boldsymbol{u}} H(t, \boldsymbol{x}^*(t), \boldsymbol{u}^*(t), \boldsymbol{J}^*_{\boldsymbol{x}}(t)) \dot{\boldsymbol{u}} + \nabla_{\boldsymbol{J_x}} H(t, \boldsymbol{x}^*(t), \boldsymbol{u}^*(t), \boldsymbol{J}^*_{\boldsymbol{x}}(t)) \dot{\boldsymbol{J}}_{\boldsymbol{x}},\ \forall t \in [t_0, t_f^*] \end{aligned} \tag{2.48}$$

From conditions 2 and 4 of Theorem 1 and from condition (2.46), one can simplify (2.48) to

$$\dot{H}(t, \boldsymbol{x}^*(t), \boldsymbol{u}^*(t), \boldsymbol{J}^*_{\boldsymbol{x}}(t)) = \frac{\partial H(t, \boldsymbol{x}^*(t), \boldsymbol{u}^*(t), \boldsymbol{J}^*_{\boldsymbol{x}}(t))}{\partial t},\ \forall t \in [t_0, t_f^*] \tag{2.49}$$

If the Hamiltonian is not explicitly dependent on time t, then

$$\frac{\partial H(t, \boldsymbol{x}^*(t), \boldsymbol{u}^*(t), \boldsymbol{J}^*_{\boldsymbol{x}}(t))}{\partial t} = 0,\ \forall t \in [t_0, t_f^*] \tag{2.50}$$

which, from (2.49), yields

$$\dot{H}(t, \boldsymbol{x}^*(t), \boldsymbol{u}^*(t), \boldsymbol{J}^*_{\boldsymbol{x}}(t)) = 0,\ \forall t \in [t_0, t_f^*] \tag{2.51}$$

which means that, in the case where the Hamiltonian does not explicitly depend on time, the Hamiltonian is constant.

Therefore, the Hamiltonian for all time is equal to its final value

$$H(t) = H(t_f^*) = -\frac{\partial \boldsymbol{\Phi}(t_f^*, \boldsymbol{x}^*(t))}{\partial t_f},\ \forall t \in [t_0, t_f^*] \tag{2.52}$$

If

$$\frac{\partial \boldsymbol{\Phi}(t_f^*, \boldsymbol{x}^*(t))}{\partial t_f} = 0 \tag{2.53}$$

then

$$H(t) = H(t_f^*) = 0, \ \forall t \in [t_0, t_f^*] \tag{2.54}$$

which means that H is constant and conserved.

2.5 Descartes' Rule of Signs

Sometimes, the optimal control input may be one of the roots of a polynomial. For polynomials of degree five and above, no general formula exists to find its roots. However, one can use Descartes' Rule of Signs [79] to determine the number of positive real roots which can help determine how many roots are valid solutions of the optimal control problem.

Theorem 2 (Descartes' Rule of Signs [79])**.** *The number of positive real roots of a polynomial does not exceed the number of sign changes of its coefficients and differs from it by a multiple of two.*

Corollary 1 (Descartes' Rule of Signs - Negative Real Roots [79])**.** *The number of negative real roots of a polynomial $f(x)$ does not exceed the number of sign changes of the coefficients of the polynomial $f(-x)$ and differs from it by a multiple of two.*

Knowing the number of positive and negative real roots allows one to determine the number of imaginary roots.

Example 1. *Consider the fourth-degree polynomial*

$$f(x) = x^4 + x^2 - 2 \tag{2.55}$$

with a positive real root at $x = 1$, a negative real root at $x = -1$, and a pair of complex roots at $x = \sqrt{2}i$ and $x = -\sqrt{2}i$. Using Theorem 2, one counts the number of sign changes to be

1. Therefore, one should expect exactly 1 positive real root. Then, using Corollary 1, one counts the number of sign changes for $f(-x)$ to be 1. As a result, one should expect exactly 1 negative real root. Since there are exactly 1 positive and 1 negative real root, then there must be 2 complex roots.

Example 2. *Consider the fifth-degree polynomial*

$$g(x) = x^5 - x^4 - 16x + 16 \tag{2.56}$$

with two positive real roots at $x = 1$ and $x = 2$, a negative real root at $x = -2$, and a pair of complex roots at $x = 2i$ and $x = -2i$. From Theorem 2, one counts the number of sign changes to be 2. Therefore, one should expect either 0 or 2 positive real roots. Then, using Corollary 1, one counts the number of sign changes for $g(-x)$ to be 1. As a result, one should expect exactly 1 negative real root. Hence, one gets the two following possible situations

- *Situation 1: 0 positive real, 1 negative real, and 4 complex roots.*
- *Situation 2: 2 positive real, 1 negative real, and 2 complex roots.*

2.6 Shooting Method

The shooting method is used to numerically solve two-point boundary value problems (2PBVPs) by reducing them to initial value problems (IVP). A two-point boundary value problem is composed of a set of ordinary differential equations (ODEs), and initial and final conditions known as boundary conditions [80].

Consider a set of q first-order ODEs with initial and final conditions.

$$\begin{aligned} &\dot{\boldsymbol{\xi}} = f(t, \boldsymbol{\xi}(t)) \\ &\xi_i(t_0) = \xi_0, \ i = 1, ..., p \\ &\xi_j(t_f) = \xi_f, \ j = p+1, ..., q \end{aligned} \tag{2.57}$$

The shooting method guesses the missing initial conditions until a trajectory is found so that it meets the desired final conditions. The shooting method stops when the error ϵ_j between the final conditions and the final states reached by guessing the initial conditions is smaller than a tolerance defined a priori.

The pseudo-code for an example of a typical shooting method algorithm where $\xi^{[k]}(t)$ is the state trajectory at the kth-iteration is presented below.

Algorithm 1 Shooting Method

1. **Starting Point:** Initial guess for $\xi_j^{[0]}(t_0)$ for values of j where the initial state is missing, initialize $k = 0$, define a tolerance tol, a maximum number of iterations k_{max}, and a step size b.
2. **Loop:**
   (a) Simulate the system using a numerical method for IVPs.
   (b) Compute $\epsilon_j = \xi_j^{[k]}(t_f) - \xi_j(t_f)$.
   (c) Update $\xi_j^{[k+1]}(t_0) = \xi_j^{[k]}(t_0) - b\epsilon_j$, for values of j where the initial state is missing.
   (d) Update $k = k + 1$.
3. **Stopping Criterion:** Stop if $|\epsilon_j| < tol$ or $k \geq k_{max}$.

In the context of the work in this thesis, the simulated system is composed of the state and of the co-states dynamics.

Chapter 3

Optimal DOC for Hybrid-Electric Aircraft in Cruise without Wind

3.1 Introduction

As per a NASA analysis of global temperatures [81], the year 2020 tied with the year 2016 for the warmest year on record. Despite a pandemic which slowed down the global economy, greenhouse gases emissions have not reduced significantly enough to avoid the climate crisis the world is facing. However, a new wave of initiatives and commitments to curb the climate crisis led by world governments and industry leaders has risen over the past year. Such efforts stem from a wide range of industrial sectors such as the energy and transportation industries. A notable participant in such efforts is the civil aviation industry. Over the past year, two of the world's leading aircraft manufacturers, Airbus and Boeing, stepped forward to develop carbon-neutral aircraft. Airbus plans to develop a series of hybrid-electric aircraft fueled by hydrogen named ZEROe by 2035 [82]. In contrast, Boeing intends to develop aircraft completely fueled by bio-fuels [83]. Many other aircraft manufacturers [84] have announced plans to develop or are developing carbon-neutral aircraft such as Faradair Aerospace, Heart Aerospace, Wright Electric, and Zunum Aero.

Main contenders to replace conventional aircraft are hybrid-electric aircraft. This type of aircraft uses both fuel and electricity as sources of energy for flight. As a result, the hybrid-electric aircraft can help airlines achieve their sustainability goals while maintaining aircraft performance and range comparable to conventional aircraft.

This chapter presents a method to minimize the direct operating cost (DOC) of a hybrid-electric aircraft in steady cruise flight using the longitudinal flight dynamics of the aircraft assuming a weak or zero wind field. The chapter will be organized as follows. First, the optimal DOC problem will be formulated for hybrid-electric aircraft in steady cruise flight without wind. A solution is then proposed for this problem based on the Pontryagin minimum principle (PMP). Simulations are then performed to study the effects of different time costs, energy costs, and level of hybridization on aircraft performance. Finally, with the growing interest of the civil aviation sector towards hydrogen hybrid-electric aircraft, a case study of this type of hybrid-electric aircraft will be performed and compared to the case of a kerosene-fuel hybrid-electric aircraft.

3.2 Problem Statement

The dynamic model of the hybrid-electric aircraft is based on the longitudinal flight dynamics (2.25)-(2.28) presented in Chapter 2. As the aircraft propulsion system is hybrid, the fuel consumption is given by (2.35) with the thrust produced by the jet engines given by (2.36) and the electricity consumption is given by (2.39).

The dynamic model of the hybrid-electric aircraft can be simplified by making the following assumptions:

1. The lateral dynamics of the aircraft are not considered, i.e., $\dot{y} = \dot{\psi} = \dot{\phi} = \psi = \phi = 0$.
2. The wind is assumed to be weak, therefore its effects can be neglected.
3. The aircraft is in steady cruise flight at a constant altitude, i.e., $\dot{\gamma} = \gamma = \dot{h} = 0$, and air density is constant.

4. The angle of attack of the aircraft is small. Therefore, we can approximate $\cos\alpha \approx 1$, and $\sin\alpha \approx \alpha$.

5. It is assumed that the flight Mach number will be below the drag divergence Mach number. As a result, compressibility drag divergence does not need to be considered.

6. The thrust perpendicular to the velocity is small compared to weight and lift ($T\sin\alpha \ll W$ and $T\sin\alpha \ll L$).

7. The thrust specific fuel consumption in cruise is assumed to be a function of the altitude h (i.e. $S_{fc} = S_{fc}(h)$).

8. The output voltage does not vary much with the state of charge, i.e., it stays within the nominal zone shown in Figure 3.1, which is based on the Shepherd model for battery discharge [85].

9. The internal resistance of the battery is small and can thus be neglected. Its effects can be integrated into the system through a slight reduction in the electrical system efficiency η.

10. The battery temperature remains within an acceptable range and thermal effects on the battery can be neglected.

11. The hybridization coefficient β is assumed to remain constant and is given a priori.

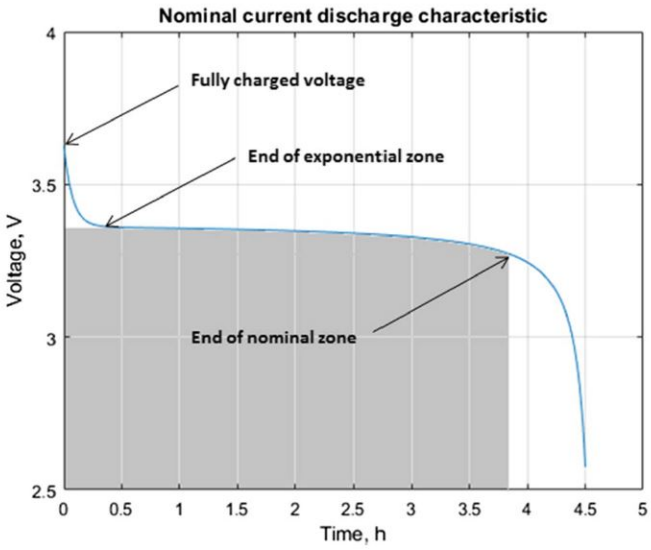

Figure 3.1: Nominal current discharge of a typical lithium-ion battery. [3]

Under the above assumptions, the simplified dynamic model of the hybrid-electric aircraft is

$$T = D \tag{3.1}$$

$$L = W \tag{3.2}$$

$$\dot{x} = v \tag{3.3}$$

$$\dot{W} = -(1-\beta)S_{fc}D = -f \tag{3.4}$$

$$\dot{Q} = -\frac{\beta D v}{\eta U} = -i \tag{3.5}$$

where the drag force D is defined by (2.7), f is the fuel flow rate, and i is output current of the battery.

3.3 Problem Formulation and Solution

The direct operating cost (DOC) can be written as

$$DOC = \int_0^{t_f} (C_t + C_i \kappa_i U i + C_f \kappa_f f) dt \tag{3.6}$$

where C_t, C_i, and C_f are the time-related costs, electrical energy cost, and fuel energy cost, respectively and t_f is the final time. The coefficient $\kappa_i = 2.78 \times 10^{-7}$ converts Joules to kilowatt-hours and the coefficient $\kappa_f = eg^{-1}$ is another conversion factor, where e is the heating value of fuel (energy per unit mass) in kWh/kg, and g is the gravitational acceleration in ms^{-2}. We now define two coefficients

$$C_\mu = \frac{C_i + C_f}{2} \tag{3.7}$$

$$C_\Delta = \frac{C_i - C_f}{2} \tag{3.8}$$

which represent the average of the two energy costs and a half of the difference between them, respectively.

For $C_\mu > 0$, minimizing the DOC is equivalent to minimizing the cost functional

$$J = \int_0^{t_f} \left(C_I + (1 + C_E)\kappa_i U i + (1 - C_E)\kappa_f f\right) dt \tag{3.9}$$

where $C_I = C_t/C_\mu$ is a trade-off parameter between time-related costs and the average energy cost, and $C_E = C_\Delta/C_\mu$ is the ratio between differential and common modes for the energy cost and, therefore, $-1 \leq C_E \leq 1$.

The optimal control problem based on (3.1)-(3.5), (2.7), and (3.9) can be formulated as

$$\begin{aligned} J^*(x_0) = &\min_{v,t_f} \int_0^{t_f} (C_I + (1+C_E)\kappa_i U i + (1-C_E)\kappa_f f)dt \\ &s.t. \\ &\dot{x} = v \\ &\dot{W} = -(1-\beta)S_{fc}D = -f \\ &\dot{Q} = -\frac{\beta D v}{\eta U} = -i \\ &D = \frac{1}{2}C_{D,0}\rho S v^2 + \frac{2C_{D,2}W^2}{\rho S v^2} \\ &x(0) = 0,\ x(t_f) = x_f \\ &W(0) = W_0,\ Q(0) = Q_0 \end{aligned} \tag{3.10}$$

Theorem 3. *The optimal solution of the optimal control problem (3.10) v^* is a positive real root of the quintic equation*

$$\begin{aligned} &\frac{\rho^2 S^2 C_{D,0}\beta(1+C_E)\kappa_i}{\eta}{v^*}^5 + \frac{\rho^2 S^2 C_{D,0}(1-\beta)S_{fc}\bar{J}_W^*}{2}{v^*}^4 - C_I\rho S{v^*}^2 \\ &- \frac{4C_{D,2}W^2\beta(1+C_E)\kappa_i}{\eta}v^* - 6C_{D,2}W^2\bar{J}_W^* S_{fc} = 0 \end{aligned} \tag{3.11}$$

where

$$\bar{J}_W^* = (1-C_E)\kappa_f - J_W^* \tag{3.12}$$

and the time derivative of J_W^* is given by

$$\dot{J}_W^* = -\beta(1+C_E)\kappa_i\frac{4C_{D,2}W}{\eta\rho S v^*} - (1-\beta)\bar{J}_W^* S_{fc}\frac{4C_{D,2}W}{\rho S {v^*}^2} \tag{3.13}$$

with final condition

$$J_W^*(t_f) = 0 \tag{3.14}$$

If $\bar{J}_W^* \geq 0$, there is a single positive real root. If $\bar{J}_W^* < 0$, there can be either zero or two

positive real roots.

Proof. From (3.10), one can formulate the Hamiltonian of the optimal control problem as

$$H = C_I + (1 + C_E)\kappa_i U i + (1 - C_E)\kappa_f f + J_x^* \dot{x} + J_Q^* \dot{Q} + J_W^* \dot{W} \tag{3.15}$$

where J_x^*, J_W^*, and J_Q^* are the partial derivatives of the optimal cost-to-go with respect to longitudinal position x, weight W, and electric charge Q, respectively. From $\dot{x} = v$ and state equations (3.4) and (3.5), one can rewrite (3.15) as

$$H = C_I + \bar{J}_Q^* \frac{\beta D v}{\eta U} + \bar{J}_W^* (1 - \beta) S_{fc} D + J_x^* v \tag{3.16}$$

where

$$\bar{J}_Q^* = (1 + C_E)\kappa_i U - J_Q^* \tag{3.17}$$

and $\bar{J}_W^*$ is given by (3.12). One can define the terminal condition Ψ as

$$\Psi = x(t_f) - x_f = 0 \tag{3.18}$$

The transversality conditions are then

$$H(t_f) = 0 \tag{3.19}$$

$$J_Q^*(t_f) = \nu \frac{\partial \Psi}{\partial Q}\bigg|_{t_f} = 0 \tag{3.20}$$

$$J_W^*(t_f) = \nu \frac{\partial \Psi}{\partial W}\bigg|_{t_f} = 0 \tag{3.21}$$

where ν is a Lagrange multiplier.

The Hamilton's equations for the co-states are

$$\dot{J}_x^* = -\frac{\partial H}{\partial x} = 0 \tag{3.22}$$

$$\dot{J}_Q^* = -\frac{\partial H}{\partial Q} = 0 \tag{3.23}$$

$$\dot{J}_W^* = -\frac{\partial H}{\partial W} = -\bar{J}_Q^* \beta \frac{D_W v}{\eta U} - \bar{J}_W^* (1-\beta) S_{fc} D_W \tag{3.24}$$

where D_W is the partial derivative of the drag force D with respect to the weight W. From (3.22) and (3.23), one can observe that the co-states J_x^* and J_Q^* are constant. Therefore, the co-state J_Q^* is equal to its final condition (3.20),

$$J_Q^*(t) = 0, \ \forall t \in [0, t_f] \tag{3.25}$$

Replacing (3.25) into (3.17), one can write

$$\bar{J}_Q^* = (1 + C_E)\kappa_i U \tag{3.26}$$

From (3.16) and Pontryagin's minimum principle [77], the first-order necessary condition for a minimum is

$$\frac{\partial H}{\partial v} = \frac{\bar{J}_Q^* \beta}{\eta U}(D_v v + D) + \bar{J}_W^* (1-\beta) S_{fc} D_v + J_x^* = 0 \tag{3.27}$$

where D_v is the partial derivative of the drag D with respect to the airspeed v. Based on (3.26) and on the necessary condition (3.27), one can derive an expression for the co-state J_x^* as

$$J_x^* = -\frac{(1 + C_E)\kappa_i \beta}{\eta}(D_v v + D) - \bar{J}_W^* (1-\beta) S_{fc} D_v \tag{3.28}$$

The second-order necessary condition for a minimum is

$$\frac{\partial^2 H}{\partial v^2} = \frac{(1 + C_E)\kappa_i \beta}{\eta}(D_{vv} v + 2D_v) + \bar{J}_W^* (1-\beta) S_{fc} D_{vv} \geq 0 \tag{3.29}$$

where D_{vv} is the second-order partial derivative of the drag D with respect to the airspeed v. Using the drag model (2.7), one can write

$$D_v = \rho S C_{D,0} v - \frac{4 C_{D,2} W^2}{\rho S v^3} \tag{3.30}$$

$$D_{vv} = \rho S C_{D,0} + \frac{12 C_{D,2} W^2}{\rho S v^4} \tag{3.31}$$

$$D_W = \frac{4 C_{D,2} W}{\rho S v^2} \tag{3.32}$$

From (3.31), one can conclude that $D_{vv} > 0$, which means that the drag function is strictly convex on the variable v.

From (2.49) and since the Hamiltonian does not depend explicitly on time, one can write

$$\dot{H} = \frac{\partial H}{\partial t} = 0 \tag{3.33}$$

and hence, using (3.19)

$$H(t) = H(t_f) = 0, \ \forall t \in [0, t_f] \tag{3.34}$$

Substituting (2.7), (3.26), (3.28), and (3.30) into the Hamiltonian (3.16) and using (3.34), one obtains the quintic equation (3.11). A candidate for the solution of the optimal control problem in (3.10) must be a strictly positive real root of (3.11).

As $\bar{J}_W^*$ can be either positive or negative, one finds two different scenarios when applying the Descartes' Rules of Sign in Theorem 2 to the quintic equation (3.11).

1. If $\bar{J}_W^* \geq 0$, one counts the number of sign changes to be exactly one and there is a single positive real root.

2. If $\bar{J}_W^* < 0$, one counts the number of sign changes to be two, which means that there are either zero or two positive real roots.

□

3.4 Simulations Results

3.4.1 Shooting Method

Based on (3.10), (3.12), (3.13), and (3.21), one obtains the augmented system

$$\begin{aligned}
&\dot{x} = v \\
&\dot{Q} = -\frac{\beta D v}{\eta U} \\
&\dot{W} = -(1-\beta) S_{fc} D \\
&\dot{J}_W^* = -\frac{4(1+C_E)\kappa_i \beta C_{D,2} W}{\eta \rho S v} - \bar{J}_W^*(1-\beta) S_{fc} \frac{4 C_{D,2} W}{\rho S v^2} \\
&x(0) = x_0,\ x(t_f) = x_f \\
&Q(0) = Q_0,\ W(0) = W_0 \\
&J_W^*(t_f) = 0 \\
&v > 0
\end{aligned} \tag{3.35}$$

The objective of the shooting method is to find an initial condition $J_W^*(0)$ for a trajectory which satisfies the final condition (3.21). Algorithm 2 describes the shooting method used in this section.

Algorithm 2 Shooting Method

1. **Starting Point**:
   (a) Provide an initial guess for $J_W^*(0)$.
   (b) Initialize the parameter $k = 0$.
   (c) Define a tolerance tol, a maximum number of iterations k_{max}, and step size b.
2. **Loop**:
   (a) Simulate (3.35) using a numerical method for ordinary differential equations where the airspeed v is obtained using (3.11) and a root-finding method. Only the strictly positive real root of (3.11) is chosen.
   (b) Compute $\epsilon = {J_W^*}^{[k]}(t_f) - J_W^*(t_f)$.
   (c) Update ${J_W^*}^{[k+1]} = {J_W^*}^{[k]} - b\epsilon$.
   (d) Update $k = k + 1$.
3. **Stopping Criterion**: Stop if $|\epsilon| < tol$ or $k \geq k_{max}$.

This algorithm will be applied to the cases of a small unmanned aircraft, a large commercial aircraft, and a hydrogen hybrid-electric aircraft. For the simulations, the shooting method parameters are chosen to be

$$\begin{aligned} tol &= 10^{-18} \\ k_{max} &= 10 \\ b &= 1 \end{aligned} \tag{3.36}$$

3.4.2 Summary of Results

The simulation results are summarized in Table 3.1. They are obtained based on the augmented system (3.35) and on Theorem 3. The shooting method of Algorithm 2 is used for the simulations.

Table 3.1: Simulation results summary

Experiment	**Results**
v^* as a function of C_I	Small unmanned aircraft: Figure 3.3 Large commercial aircraft: Figure 3.6
Pareto-optimal trade-off curves	Small unmanned aircraft: Figure 3.4 Large commercial aircraft: Figure 3.7
Energy consumption, flight duration, and DOC as a function of β	Small unmanned aircraft: Figure 3.5 Large commercial aircraft: Figure 3.8
Lowest cost β for different C_E	Table 3.6
Comparison between Algorithm 2 and `bvp5c`	Table 3.4

3.4.3 Small Unmanned Aircraft

The model of NASA's GL-10 Greased Lightning hybrid-electric aircraft will be used in the simulations. The aircraft model parameters are presented in Table 3.2. For the purpose of the simulations, it is assumed that the aircraft carry the necessary charge for the entire flight.

Table 3.2: NASA GL-10 Greased Lightning technical data

Parameter	Value
Wing area	0.737 m^2
Lift-to-drag ratio	7.2
Maximum take-off weight	28.1 kg
Empty weight	20.9 kg
Specific fuel consumption[a]	1.1×10^{-5} kg/(N·s)
Fuel type	Diesel
Fuel energy density	12.6 kW·h/kg
Battery system	Four flight batteries
Battery type	Lithium polymer cells
Battery capacity	4.34 A·h
Battery system voltage	28 V
Electrical system efficiency[a]	0.68
Zero-lift drag coefficient[a]	0.025
Induced drag coefficient[a]	0.193

[a] Estimates

The zero-lift drag coefficient $C_{D,0}$ is chosen to be 0.025 as it is within range of a typical general aviation aircraft [86]. The induced drag coefficient $C_{D,2}$ is estimated based on the

lift-to-drag ratio [69]

$$L/D = \frac{1}{2}\sqrt{\pi Ae/C_{D,0}}$$
$$C_{D,2} = 1/(\pi Ae) \tag{3.37}$$

where A is the aspect ratio, and e is the efficiency factor. Solving for the two unknowns $C_{D,2}$ and πAe in (3.37), one obtains the induced drag coefficient $C_{D,2} = 0.193$. The electrical system efficiency η is chosen to be 0.68 according to [87] which represents the electrical system efficiency from battery to propellers.

3.4.3.1 Effects of Different C_E

The simulation parameters to study the effects of different values of C_E on the aircraft performance are found in Table 3.3. The altitude is chosen to be 100 m to remain within the Canadian maximum altitude regulation for Remotely Piloted Aircraft Systems [88]. The distance traveled is selected to be 50 km which corresponds to the distance between the easternmost and westernmost points of Montréal Island in Québec, Canada as shown in Figure 3.2.

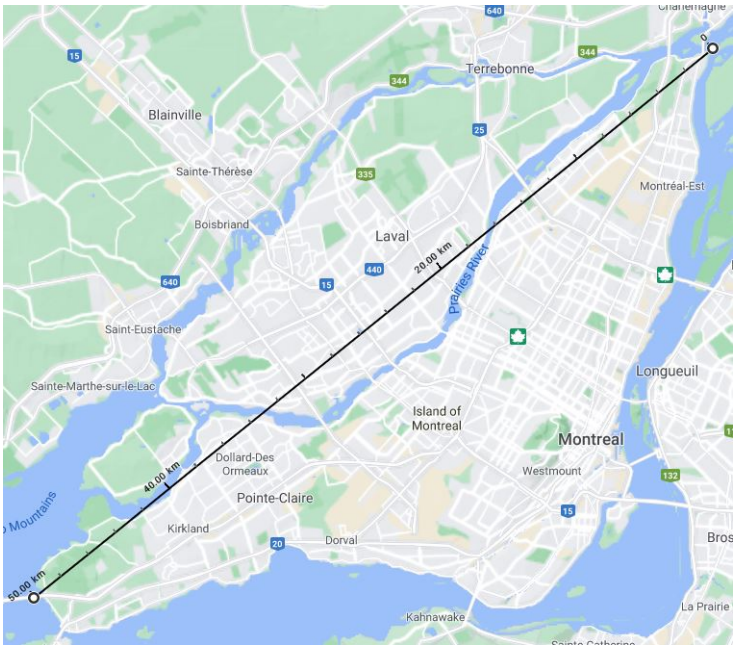

Figure 3.2: Distance between the easternmost and westernmost point of Montréal Island (taken from Google Maps [4])

The initial weight is chosen to be 275 N which corresponds to a little bit less than the maximum take-off weight of the aircraft. The initial charge is chosen to be $62,496$ C which corresponds to the battery capacity of the aircraft. Finally, the hybridization coefficient is fixed at 0.5 so that the proportion of the thrust coming from electrical energy is the equal to that coming from fuel energy.

Table 3.3: Simulation parameters

Parameter	Value
Air density (100 m)	1.225 kg/m^3
Initial position x_0	0 km
Final position x_f	50 km
Initial charge Q_0	62,496 C
Initial weight W_0	275 N
Hybridization coefficient β	0.5

Based on the aircraft model parameters and simulation parameters of Tables 3.2 and 3.3 and the shooting method in Algorithm 2, one can investigate the response of the aircraft optimal cruise airspeed to a change in C_I as shown in Figure 3.3. The simulations are performed for values of C_I ranging from 0 to 0.01 for different values of C_E. A negative C_E means that the fuel cost coefficient C_f is greater than the electricity cost coefficient C_i. Conversely, a positive C_E means that the electricity cost is greater than the fuel cost coefficient. If $C_E = 0$, the electricity and fuel cost coefficients are equal. The quintic equation (3.11) is used to compute the optimal cruise airspeed. Its strictly positive real roots are found using a root-finding method. The all-electric [3] and all-fuel [5] economy mode solutions are shown as a comparison in Figure 3.3 at the initial and final positions, respectively.

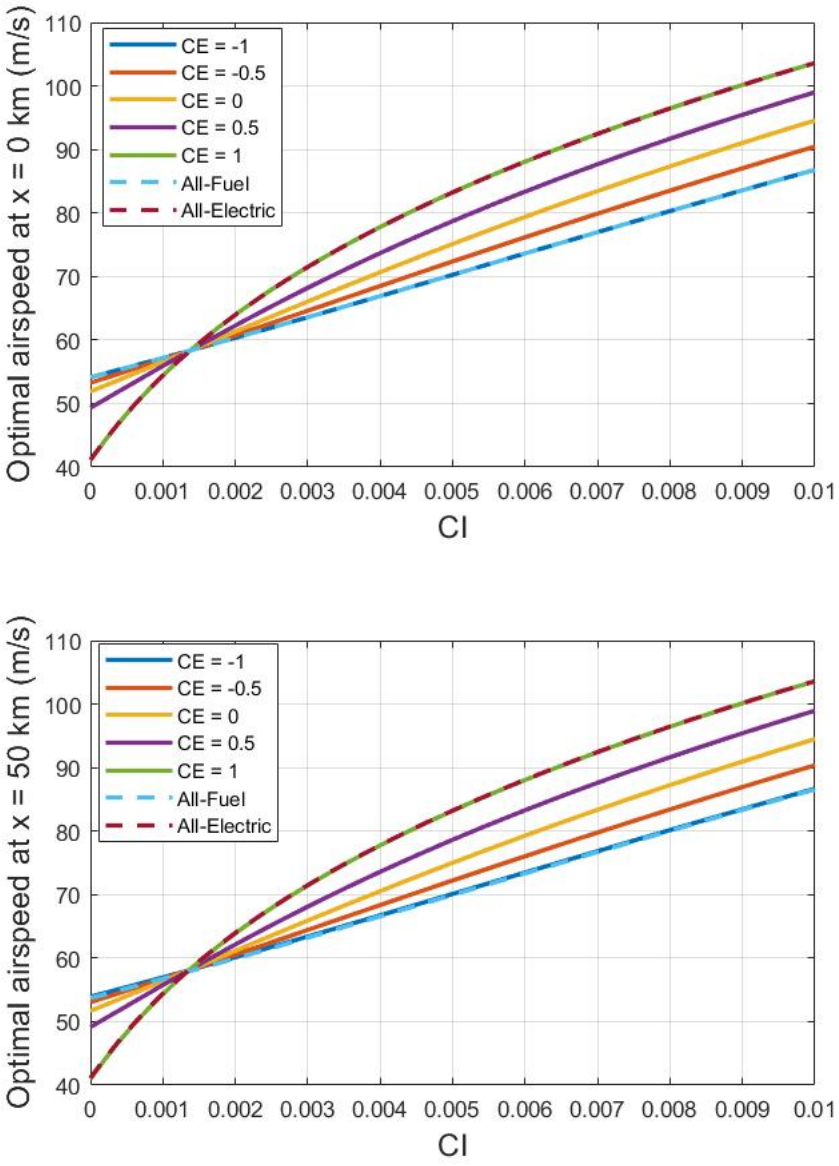

Figure 3.3: Optimal cruise airspeed $v^*(t_0)$ and $v^*(t_f)$ as a function of C_I when $C_E = -1$, $C_E = -0.5$, $C_E = 0$, $C_E = 0.5$, and $C_E = 1$ compared to the all-electric and all-fuel solutions of [3] and [5]

From Figure 3.3, one can observe that as C_I grows, the optimal cruise airspeed increases for all six scenarios in the above figure. As C_I increases, the time-related costs increases relative to the average energy cost. In other words, the cost per unit of time becomes more expensive relative to the cost per unit of energy. Therefore, the aircraft should fly faster to

compensate for the larger time cost which is what one sees in Figure 3.3.

Additionally, in Figure 3.3, one can observe that the fuel economy mode follows closely the trajectory of $C_E = -1$, while the all-electric economy mode follows closely the trajectory of $C_E = 1$. As the cost of fuel increases relative to the cost of electricity, one can expect the system to choose to minimize the fuel cost more and therefore, the solution should converge towards the fuel economy mode solution. Similarly, as the cost of electricity increases relative to the cost of fuel, one can expect the system to choose to minimize the electricity cost more and, as a result, the solution should converge towards the all-electric economy mode. One can see the convergence towards the fuel and all-electric economy by observing the trajectories created when $C_E = -0.5$, $C_E = 0$, and $C_E = 0.5$. When $C_E = -0.5$, one can observe that the trajectory is between that of $C_E = -1$ and $C_E = 0$. Similarly, for $C_E = 0.5$, one can see that the trajectory is between that of $C_E = 0$ and $C_E = 1$.

To validate the results obtained using the shooting method, the MATLAB built-in boundary-value problem solver `bvp5c` is used. The two methods are compared for different pairs of C_I and optimal final cruise airspeed at $C_E = 0$ in Table 3.4. The percent difference is computed using the following equation

$$\%\ Diff = \frac{|v^*_{shooting}(t_f) - v^*_{bvp5c}(t_f)|}{\frac{v^*_{shooting}(t_f)+v^*_{bvp5c}(t_f)}{2}} \times 100 \tag{3.38}$$

where $v^*_{shooting}(t_f)$ and $v^*_{bvp5c}(t_f)$ are the final optimal cruise airspeed $v^*(t_f)$ computed using Algorithm 2 and `bvp5c`, respectively.

Table 3.4: Comparison between Algorithm 2 and `bvp5c`

	$v^*_{shooting}(t_f)$ (m/s)	$v^*_{bvp5c}(t_f)$ (m/s)	% Diff
$C_I = 0$	51.69451	51.69439	2.146×10^{-4}
$C_I = 0.001$	56.37715	56.37714	2.298×10^{-6}
$C_I = 0.01$	94.495595	94.49559	5.107×10^{-6}

From Table 3.4, one can observe that the results obtained using `bvp5c` match closely those obtained using the shooting method.

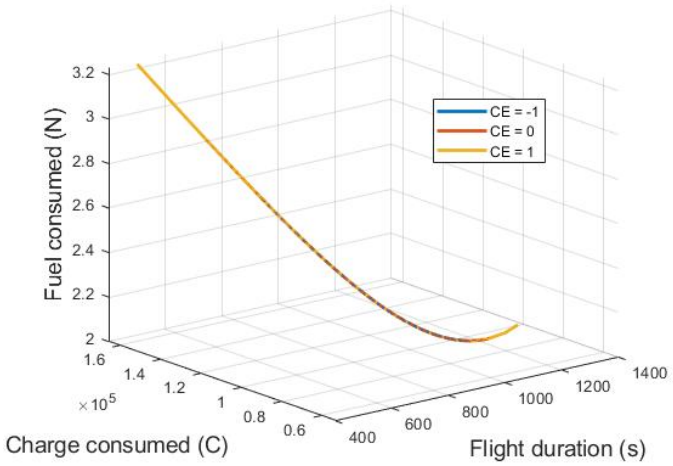

Figure 3.4: Pareto-optimal trade-off curves for NASA GL-10 Greased Lightning.

From the Pareto-optimal trade-off curve of Figure 3.4, one can observe that as the optimal cruise flight duration decreases, the optimal electricity and fuel consumption increases. Such a result is expected since a shorter flight duration corresponds to a greater cruising airspeed when the distance travelled is fixed. Therefore, by flying faster, the aircraft will consume more energy. Furthermore, a decrease in the flight duration is a consequence of an increase in time-related costs. From Figure 3.3, we saw that an increase in C_I yields an increase in the optimal cruise airspeed which translates into a decrease in flight duration, which further supports the results shown in Figure 3.4.

3.4.3.2 Effects of Different β

The simulation parameters to study the effects of different values of β on the aircraft performance are found in Table 3.5. The values for the parameters in Table 3.5 differ from those of Table 3.3. Previously, to evaluate the effects of varying C_E, β was fixed. Now, to evaluate the effects of varying β, the cost coefficients are fixed. The electricity cost coefficient of 0.06 CAD/kWh is chosen based on Hydro-Québec's rates [89]. The fuel cost coefficient is chosen be 0.06 CAD/kWh based on the average price of diesel in early 2020 [90]. The time-related cost coefficient is chosen to be 0.0006 CAD/s to yield a C_I of 0.01 as $C_I = 2C_t/(C_i + C_f)$.

Table 3.5: Simulation parameters

Parameter	Value
Air density (100 m)	1.225 kg/m^3
Initial position x_0	0 km
Final position x_f	50 km
Initial charge Q_0	62,496 C
Initial weight W_0	275 N
Time-related cost coefficient C_t	0.0006 CAD/s
Electricity cost coefficient C_i	0.06 CAD/kWh
Fuel cost coefficient C_f	0.06 CAD/kWh

Based on the aircraft parameters listed in Table 3.2, on the simulation parameters of Table 3.5, and on the augmented system (3.35), one can compute the response of the charge and fuel consumed, the flight duration, and the direct operating cost to changes in the hybridization coefficient β as shown in Figure 3.5 using (3.4), (3.5), and (3.6).

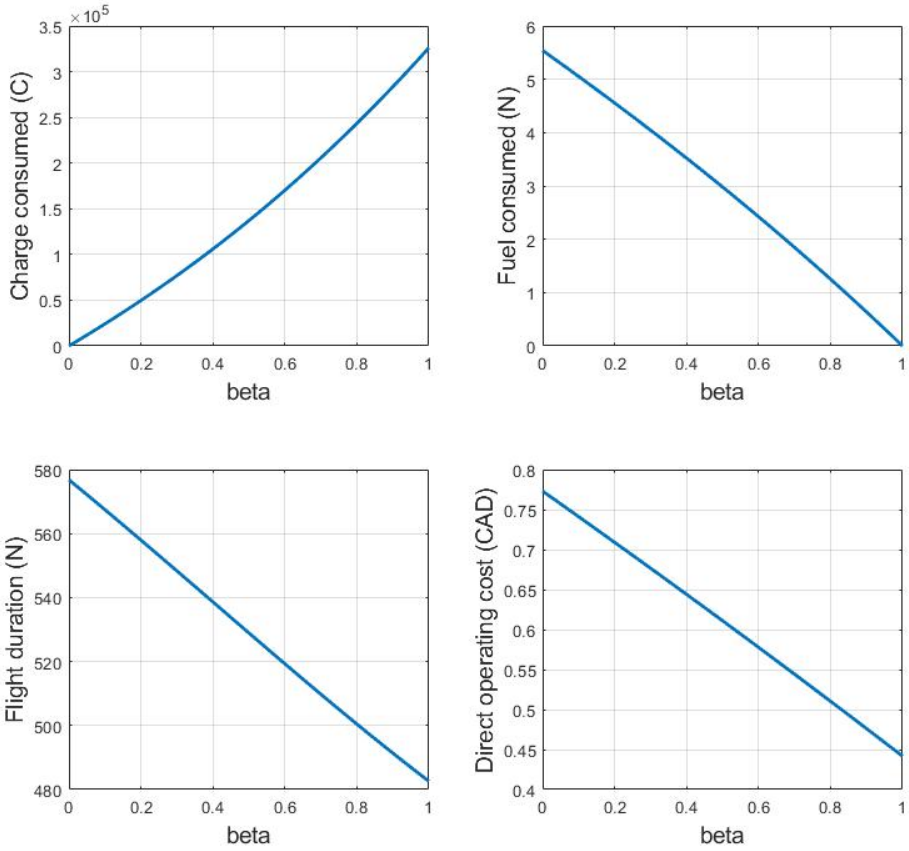

Figure 3.5: Charge and fuel consumed, flight duration, and cost as a function of β.

From Figure 3.5, one can see that the fuel consumption decreases and electricity consumption increases as β approaches one which is to be expected from the dynamics of the electric charge (3.5). Furthermore, as β approaches zero, the fuel consumption increases and the electricity consumption decreases which is expected from the fuel flow rate (3.4). Additionally, as β approaches one, the cost decreases. One can conclude that, for the simulation parameters in Table 3.5, the value of β yielding the lowest cost is one. This may suggest that the lowest DOC energy management strategy is either $\beta = 0$ or $\beta = 1$. To verify this, we change the value of C_E and see if, for a given C_E, the optimal β is zero. The pairs $C_E = -1$ and $\beta = 1$ and $C_E = 1$ and $\beta = 0$ yield infinitely many solutions as one can see if one were to replace the pairs into the quintic equation (3.11). Therefore, they are ignored in the simulations. The results of the investigation is shown in Table 3.6 where $C_I = 0.1$.

Table 3.6: Investigation of the Lowest Cost β for Different C_E

	$\beta = 0$	$\beta = 0.5$	$\beta = 1$
$C_E = -0.99$	3.37\$	2.38\$	0.44\$
$C_E = -0.9$	3.45\$	2.48\$	0.99\$
$C_E = -0.5$	3.88\$	3.06\$	2.15\$
$C_E = 0$	4.75\$	4.42\$	4.07\$
$C_E = 0.18$	3.64\$	3.69\$	3.64\$
$C_E = 0.5$	2.24\$	2.83\$	3.11\$
$C_E = 0.9$	0.79\$	2.16\$	2.65\$
$C_E = 0.99$	0.24\$	2.05\$	2.57\$

From Table 3.6, one can see that for $C_E \geq 0.18$, the cost is the lowest when $\beta = 0$ and, for $C_E < 0.18$, the lowest cost occurs when $\beta = 1$ which suggests that there may indeed be two possible solutions for β, either zero or one, for the lowest DOC energy management. A caveat to this conclusion is the limited battery capacity of the aircraft. It was discussed in the introduction of this thesis that a limiting factor in the widespread deployment of all-electric aircraft is battery capacity. From Figure 3.5, one can see that the electricity consumption exceeds $Q_0 = 62,496C$ for $\beta \geq 0.25$. As a result, based on the aircraft parameters, $\beta = 1$ may not be feasible for the distance to be travelled.

3.4.4 Large Commercial Aircraft

The model of the large commercial aircraft used to simulate the DOC solution for hybrid electric-aircraft is based on the Airbus and Rolls-Royce concept aircraft E-Fan X. For the purpose of the simulations, the aircraft carries the necessary battery energy for the whole flight at take-off. The aircraft model parameters [91][92][93] are presented in Table 3.7.

Table 3.7: Airbus E-Fan X technical data

Parameter	Value
Wing area	77.3 m^2
Maximum take-off weight	44,225 kg
Empty weight	25,645 kg
Lift-to-drag ratio	18.4
Specific fuel consumption	2.55×10^{-5} kg/(N·s)
Fuel type	Kerosene
Fuel specific energy	11.9 kW·h/kg
Battery type	Lithium polymer cells
Battery capacity	140 A·h
Battery system voltage	3,000 V
Electrical system efficiency[a]	0.68
Zero-lift drag coefficient	0.028
Induced drag coefficient	0.026

[a] Estimates

3.4.4.1 Effects of Different C_E

The simulation parameters to study the effects of different C_E are listed in Table 3.8. The aircraft is traveling the distance between Montreal-Trudeau International Airport (YUL) and Vancouver International Airport (YVR) and is cruising at an altitude of 11,000 m.

Table 3.8: Simulation parameters

Parameter	Value
Air density (11,000 m)	0.365 kg/m^3
Initial position x_0	0 km
Final position x_f	3,700 km
Initial charge Q_0	504,000 C
Initial weight W_0	431,000 N
Hybridization coefficient β	0.5

Based on the aircraft model parameters in Table 3.7 and the simulation parameters in Table 3.8, the relation between C_I and the optimal cruise airspeed v^* for the values of $C_E = -1$, $C_E = -0.5$, $C_E = 0$, $C_E = 0.5$, and $C_E = 1$ is shown in Figure 3.6 at the initial and final positions, respectively. The values of C_I used for the simulations range from 0 to 2.

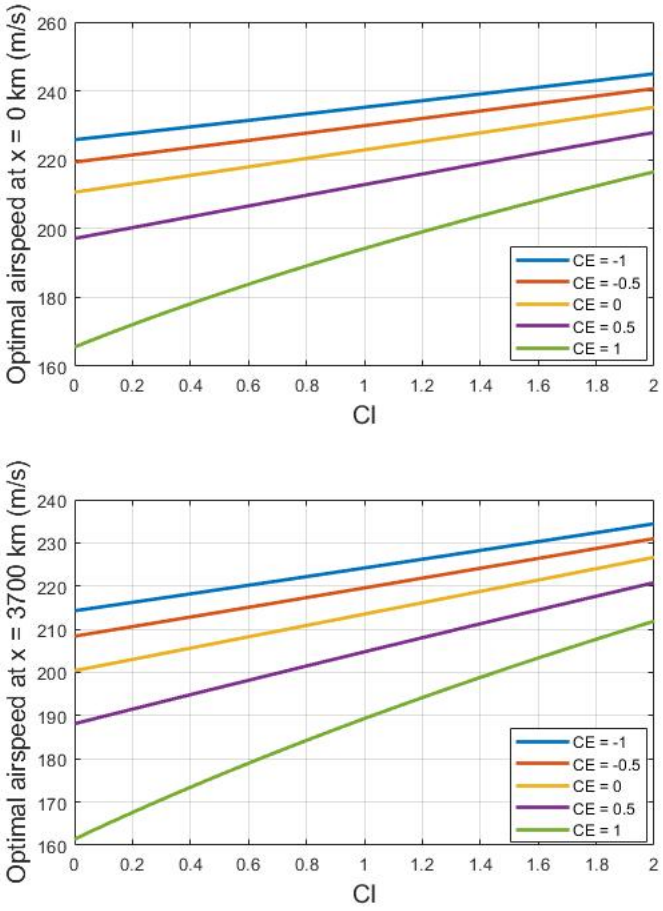

Figure 3.6: Optimal cruise airspeed $v^*(t_0)$ and $v^*(t_f)$ as a function of C_I when $C_E = -1$, $C_E = -0.5$, $C_E = 0$, $C_E = 0.5$, and $C_E = 1$.

From Figure 3.6, one can observe that, as the optimal cruise airspeed increases, C_I increases. Such a result supports the findings made previously for the small unmanned aircraft model. Furthermore, the Airbus E-Fan X is observed to fly faster than the small unmanned aircraft.

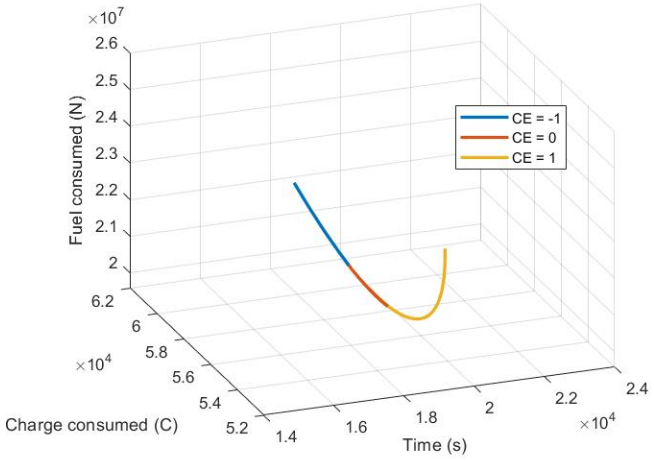

Figure 3.7: Pareto-optimal trade-off curves for the Airbus E-Fan X.

From the Pareto-optimal trade-off curves of Figure 3.7, one can see that as the optimal flight duration decreases, the energy consumption increases which further supports the findings for the small unmanned aircraft. Furthermore, one can observe that the Airbus E-Fan X consumes much more energy than the NASA GL-10 Greased Lightning, which is expected since the E-Fan X is a much larger and heavier aircraft flying at higher speeds than the NASA GL-10 Greased Lightning aircraft.

3.4.4.2 Effects of Different β

The simulation parameters to study the effects of different values of β on the aircraft performance are found in Table 3.9. The values for the parameters in Table 3.9 differ from those of Table 3.8. Previously, to evaluate the effects of varying C_E, β was fixed. Now, to evaluate the effects of varying β, the cost coefficients are fixed. The time-related cost coefficient is chosen to be 0.12 CAD/s to yield $C_I = 2$. The time cost also corresponds to a hourly rate of 432 CAD/h which is close to the average crew cost per hour for an Airbus A319 operating under Allegiant Air [94].

Table 3.9: Simulation parameters

Parameter	Value
Air density (11,000 m)	0.365 kg/m^3
Initial position x_0	0 km
Final position x_f	3,700 km
Initial charge Q_0	504,000 C
Initial weight W_0	431,000 N
Time-related cost coefficient C_t	0.12 CAD/s
Electricity cost coefficient C_i	0.06 CAD/kWh
Fuel cost coefficient C_f	0.06 CAD/kWh

Based on the aircraft parameters listed in Table 3.7 and on the simulation parameters of Table 3.9, one can compute the response of the charge and fuel consumed, the flight duration, and the direct operating cost to changes in the hybridization coefficient β as shown in Figure 3.8 using (3.4), (3.5), and (3.6).

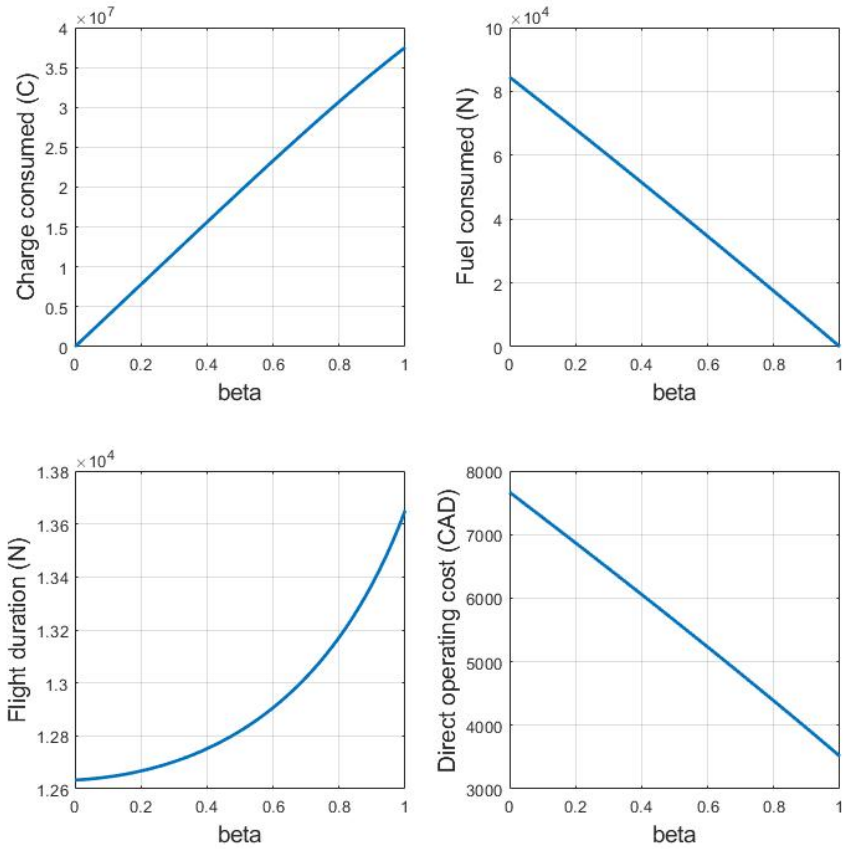

Figure 3.8: Charge and fuel consumed, flight duration, and cost as a function of β.

Similar to Figure 3.5 for the small unmanned aircraft model, Figure 3.8 shows that, as β approaches one, the electricity consumed increases and the fuel consumed decreases. Conversely, as β approaches zero, the electricity consumed decreases and the fuel consumed increases. Such a relation can also be observed in the dynamic equations of the electric charge (3.5) and the weight (3.4). Furthermore, in this scenario, $\beta = 1$ yields the lowest cost.

3.4.5 Conclusions

From the simulations presented above, one can draw the following conclusions:

- As C_I increases, the optimal cruise airspeed increases. This is shown in Figures 3.3 and 3.6.
- As the flight duration decreases, the energy consumption increases. This is shown by the Pareto-optimal curves of Figures 3.4 and 3.7.
- The shooting method in Algorithm 2 was validated using MATLAB's boundary-value problem solver `bvp5c`. This is shown in Table 3.4.
- The charge consumed increases and the fuel consumed decreases as β approaches one. Conversely, as β approaches zero, the charge consumed decreases and the fuel consumed increases. This is shown in Figures 3.5 and 3.8.
- The optimal energy management parameter β may either be when $\beta = 0$ or $\beta = 1$. This is shown in Figures 3.5 and 3.8, and Table 3.6.

3.5 Case Study with Hydrogen-Electric Aircraft

3.5.1 Comparison between the S_{fc} of Hydrogen and Kerosene Aircraft

The model of the fuel flow rate for a hydrogen jet engine [73] is defined as

$$\dot{W} = -S_{fc}T = -f \tag{3.39}$$

One can see that (3.39) is the same equation for the fuel flow rate as for a hydrocarbon-fuel aircraft (2.19). From the literature, one can find multiple studies on the thrust specific fuel consumption of hydrogen-fuel turbofan engines. The list in Table 3.10 compares the thrust specific fuel consumption of hydrogen-fuel turbofan engines from these studies to the S_{fc} of kerosene-fuel turbofan engines.

Table 3.10: Comparison between the S_{fc} of kerosene and liquid hydrogen (LH_2) fuel aircraft turbofan engines at a cruising altitude of $11,000\ m$

Engine	$S_{fc,Kerosene}\ (g/kNs)$	$S_{fc,LH_2}\ (g/kNs)$	% Difference	Reference
BR710-48	17.91	6.385	35.7	[63]
Trent 700	16	6.59	41.2	[66]
Trent 7000	14.5	5.9	40.7	[66]
CF34-8E	19	7.83	41.2	[66]
GE90	17.301	6.137	35.4	[67]
V2527-A5	15.99	5.755	36.0	[68]

From Table 3.10, one can observe that the thrust specific fuel consumption of hydrogen-fuel turbofan engines is between 35.7% and 41.2% that of a kerosene-fuel turbofan aircraft.

3.5.2 Simulation Results

For the simulations, the Airbus E-Fan X model in Table 3.7 is used with a change in the S_{fc} which is reduced by 60% following the findings in Table 3.10. The simulation parameters of Table 3.9 are used. The responses of the energy consumption, the flight duration, and the

direct operating cost to a change in β are shown in Figure 3.9.

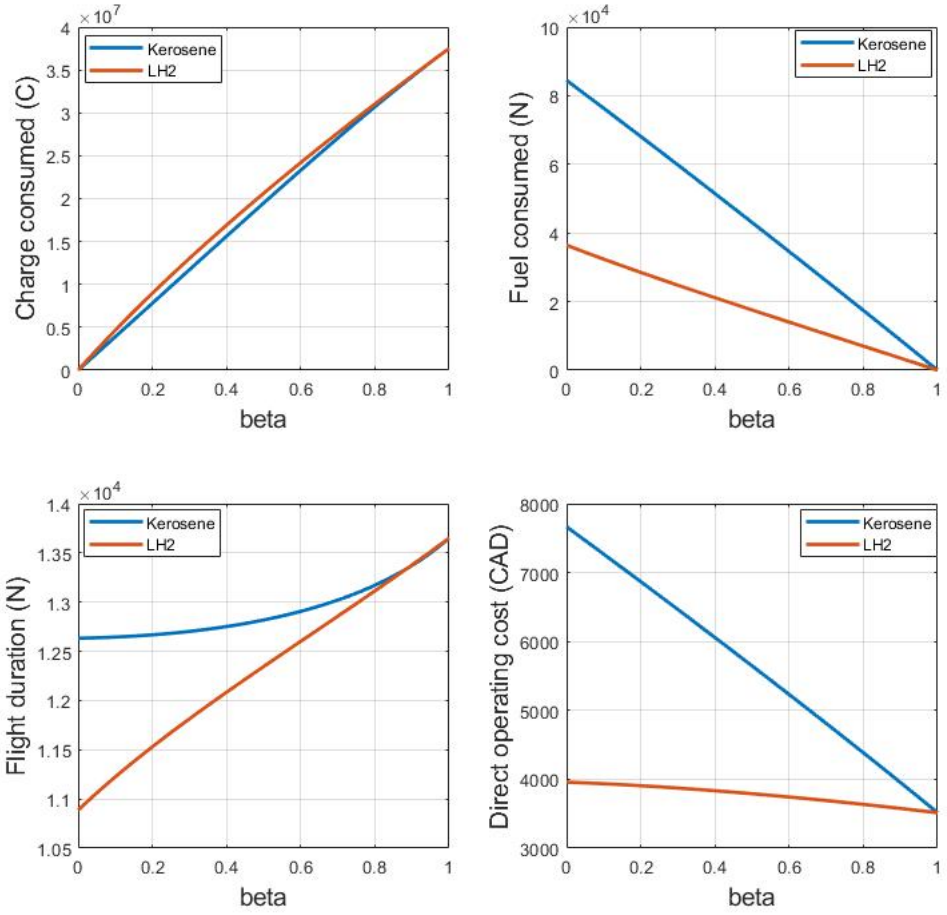

Figure 3.9: Comparison between a hydrogen-fuel and a kerosene-fuel hybrid-electric aircraft based on energy consumption, flight duration, and cost as a function of β.

In Figure 3.9, one can see that the charge consumed by the hydrogen-fuel hybrid-electric aircraft is similar to that of the kerosene-fuel aircraft. At $\beta = 0$, no electric charge is consumed by either aircraft which is expected from the dynamics of the electricity consumption (3.5). At $\beta = 1$, only electricity is consumed by both aircraft which is also expected from (3.5).

Furthermore, one can observe that the fuel consumed by the hydrogen-fuel aircraft is less than half that of the kerosene-fuel aircraft. Since the model of the fuel flow rate (3.4) and (3.39) depends on the S_{fc} and on the aircraft jet engine thrust T_{jet}, a lower S_{fc} for a

comparable T_{jet} means a smaller flow rate. Therefore, since the S_{fc} of the hydrogen-fuel aircraft is significantly smaller than that of the kerosene-fuel aircraft, one can expect that the fuel consumption of the hydrogen-fuel aircraft to be significantly less than that of the kerosene-fuel aircraft. Additionally, the fuel consumption of both aircraft converges to zero as β approaches one. Since at $\beta = 1$, from the fuel flow rate model of (3.4), the fuel flow rate is zero, then this result is expected.

Finally, one can see that the direct operating cost is significantly lower for the hydrogen-fuel hybrid-electric aircraft. Since the DOC (3.6) is a function of the fuel flow rate which is dependent on the S_{fc}, then a lower S_{fc} will lead to a lower cost. As the S_{fc} of the hydrogen-fuel aircraft is significantly lower than that of the kerosene-fuel aircraft, one should expect the direct operating cost to also be significantly lower. Furthermore, the DOC of both aircraft converges to the same value as β approaches one which is expected since the cost is a linear combination of the time-related costs, the electricity consumption, and the fuel consumption and at $\beta = 1$, the fuel consumption is zero. Therefore, at $\beta = 1$, only electricity is consumed and the DOC is only dependent on the flight duration and the electricity consumed.

Chapter 4

Optimal DOC in Constant Wind and in the Horizontal Plane

4.1 Introduction

This chapter provides an extension of the solutions in Chapter 3 to account for a constant wind field and for steady cruise flight in the horizontal plane with a constant heading. The chapter will be subdivided as follows. First, the optimal control problem will be formulated for the direct operating cost problem of a hybrid-electric aircraft in steady cruise flight in a constant wind field considering only the longitudinal flight dynamics. The solutions will be obtained using Pontryagin's minimum principle. Subsequently, simulations results will be used to investigate the effects of wind speed on the optimal cruise airspeed, the energy consumption, and on the direct operating cost. Then, the optimal control problem of Chapter 3 will be extended to the steady flight in the horizontal plane with a constant heading and the solutions will be obtained using Pontryagin's minimum principle. Simulations are then performed to verify the solutions.

The extension of the solutions in Chapter 3 to the horizontal plane stems from a change in reference frame which is useful in navigation if one were given North-East coordinates and

a heading angle. However, as one will see later in this chapter, the solutions in the horizontal place are the same as those in Chapter 3.

4.2 Optimal DOC in Constant Wind Field

4.2.1 Problem Statement

The dynamic model of the hybrid-electric aircraft is based on the longitudinal flight dynamics (2.25)-(2.28) presented in Chapter 2. As the aircraft propulsion system is hybrid, the fuel consumption is given by (2.35) with the thrust produced by the jet engines given by (2.36) and the electricity consumption is given by (2.39). Additionally, in this Chapter, the wind speed can be positive or negative. A positive wind speed indicates a tailwind and a negative wind speed represents a headwind.

The dynamic model of the hybrid-electric aircraft can be simplified by making the following assumptions:

1. The lateral dynamics of the aircraft are not considered, i.e., $\dot{y} = \dot{\psi} = \dot{\phi} = \psi = \phi = 0$.

2. The aircraft is in steady cruise flight at a constant altitude, i.e., $\dot{\gamma} = \gamma = \dot{h} = 0$, and air density is constant.

3. The angle of attack of the aircraft is small. Therefore, we can approximate $\cos\alpha \approx 1$, and $\sin\alpha \approx \alpha$.

4. It is assumed that the flight Mach number will be below the drag divergence Mach number. As a result, compressibility drag divergence does not need to be considered.

5. The thrust perpendicular to the velocity is small compared to weight and lift ($T\sin\alpha \ll W$ and $T\sin\alpha \ll L$).

6. The thrust specific fuel consumption in cruise is assumed to be a function of the altitude h (i.e. $S_{fc} = S_{fc}(h)$).

7. The output voltage does not vary much with the state of charge, i.e., it stays within the nominal zone shown in Figure 3.1, which is based on the Shepherd model for battery discharge [85].

8. The internal resistance of the battery is small and can thus be neglected. Its effects can be integrated into the system through a slight reduction in the electrical system efficiency η.

9. The battery temperature remains within an acceptable range and thermal effects on the battery can be neglected.

10. The hybridization coefficient β is assumed to remain constant and is given a priori.

Under the above assumptions, the simplified dynamic model of the hybrid-electric aircraft is

$$T = D \tag{4.1}$$

$$L = W \tag{4.2}$$

$$\dot{x} = v + v_w \tag{4.3}$$

$$\dot{W} = -(1-\beta)S_{fc}D = -f \tag{4.4}$$

$$\dot{Q} = -\frac{\beta D v}{\eta U} = -i \tag{4.5}$$

where the drag force D is defined by (2.7), v_w is the wind speed, f is the fuel flow rate, and i is output current of the battery.

4.2.2 Problem Formulation and Solution

The direct operating cost (DOC) is formulated in Chapter 3 (3.6). Minimizing the DOC is equivalent to minimizing the cost function (3.9) by defining two coefficients

$$C_E = \frac{(C_i - C_f)}{(C_i + C_f)} \tag{4.6}$$

$$C_I = \frac{2C_t}{(C_i + C_f)} \tag{4.7}$$

where C_t, C_i, and C_f are the time-related costs, electrical energy cost, and fuel energy cost, respectively and where $(C_i + C_f) > 0$.

Therefore, the optimal control problem based on (4.1)-(4.5), (2.7), and (3.9) can be formulated as

$$\begin{aligned}
J^*(x_0) = &\min_{v,t_f} \int_0^{t_f} (C_I + (1 + C_E)\kappa_i U i + (1 - C_E)\kappa_f f)dt \\
&s.t. \\
&\dot{x} = v + v_w \\
&\dot{W} = -(1 - \beta)S_{fc}D = -f \\
&\dot{Q} = -\frac{\beta D v}{\eta U} = -i \\
&D = \frac{1}{2}C_{D,0}\rho S v^2 + \frac{2C_{D,2}W^2}{\rho S v^2} \\
&x(0) = 0,\ x(t_f) = x_f \\
&W(0) = W_0,\ Q(0) = Q_0
\end{aligned} \tag{4.8}$$

Theorem 4. *The optimal solution of the optimal control problem (4.8) v^* is a positive real*

root of the sextic equation

$$\frac{(1+C_E)\kappa_i\beta\rho^2 S^2 C_{D,0}}{\eta}v^{*^6} + \left(\frac{\bar{J}_W^*(1-\beta)S_{fc}\rho^2 S^2 C_{D,0}}{2} + \frac{3(1+C_E)\kappa_i\beta\rho^2 S^2 C_{D,0}v_w}{2\eta}\right)v^{*^5}$$
$$+ \bar{J}_W^*(1-\beta)S_{fc}\rho^2 S^2 C_{D,0}v_w v^{*^4} - C_I\rho S v^{*^3} - \frac{4(1+C_E)\kappa_i\beta C_{D,2}W^2}{\eta}v^{*^2}$$
$$- \left(6\bar{J}_W^*(1-\beta)S_{fc}C_{D,2}W^2 + \frac{2(1+C_E)\kappa_i\beta C_{D,2}W^2 v_w}{\eta}\right)v^* - 4\bar{J}_W^*(1-\beta)S_{fc}C_{D,2}W^2 v_w = 0 \tag{4.9}$$

where

$$\bar{J}_W^* = (1-C_E)\kappa_f - J_W^* \tag{4.10}$$

and the time derivative of J_W^* is given by

$$\dot{J}_W^* = -\frac{4(1+C_E)\kappa_i\beta C_{D,2}W}{\eta\rho S v^*} - \bar{J}_W^*(1-\beta)S_{fc}\frac{4C_{D,2}W}{\rho S v^{*^2}} \tag{4.11}$$

with final condition

$$J_W^*(t_f) = 0 \tag{4.12}$$

Proof. From (4.8), one can formulate the Hamiltonian of the optimal control problem as

$$H = C_I + (1+C_E)\kappa_i U i + (1-C_E)\kappa_f f + J_x^*\dot{x} + J_Q^*\dot{Q} + J_W^*\dot{W} \tag{4.13}$$

where J_x^*, J_W^*, and J_Q^* are the partial derivatives of the optimal cost-to-go with respect to position x, weight W, and electric charge Q, respectively. From $\dot{x} = v + v_w$ and state equations (4.4)-(4.5), one can rewrite (4.13) as

$$H = C_I + \bar{J}_Q^*\frac{\beta D v}{\eta U} + \bar{J}_W^*(1-\beta)S_{fc}D + J_x^*(v+v_w) \tag{4.14}$$

where

$$\bar{J}_Q^* = (1+C_E)\kappa_i U - J_Q^* \tag{4.15}$$

and $\bar{J}_W^*$ is given by (4.10). One can define the terminal condition Ψ as

$$\Psi = x(t_f) - x_f = 0 \tag{4.16}$$

The transversality conditions are then

$$H(t_f) = 0 \tag{4.17}$$

$$J_Q^*(t_f) = \nu \frac{\partial \Psi}{\partial Q}\bigg|_{t_f} = 0 \tag{4.18}$$

$$J_W^*(t_f) = \nu \frac{\partial \Psi}{\partial W}\bigg|_{t_f} = 0 \tag{4.19}$$

where ν is a Lagrange multiplier.

The Hamilton's equations for the co-states are

$$\dot{J}_x^* = -\frac{\partial H}{\partial x} = 0 \tag{4.20}$$

$$\dot{J}_Q^* = -\frac{\partial H}{\partial Q} = 0 \tag{4.21}$$

$$\dot{J}_W^* = -\frac{\partial H}{\partial W} = -\bar{J}_Q^* \beta \frac{D_W v}{\eta U} - \bar{J}_W^* (1-\beta) S_{fc} D_W \tag{4.22}$$

where D_W is the partial derivative of the drag force D with respect to the weight W. From (4.20) and (4.21), one can observe that the co-states J_x^* and J_Q^* are constant. Therefore, the co-state J_Q^* is equal to its final condition (4.18),

$$J_Q^*(t) = 0, \ \forall t \in [0, t_f] \tag{4.23}$$

Replacing (4.23) into (4.15), one can write

$$\bar{J}_Q^* = (1 + C_E)\kappa_i U \tag{4.24}$$

From (4.14) and Pontryagin's minimum principle [77], the first-order necessary condition for

a minimum is

$$\frac{\partial H}{\partial v} = \frac{\bar{J}_Q^* \beta}{\eta U}(D_v v + D) + \bar{J}_W^*(1-\beta) S_{fc} D_v + J_x^* = 0 \tag{4.25}$$

where D_v is the partial derivative of the drag D with respect to the airspeed v. Based on (4.24) and on the condition (4.25), one can derive an expression for the co-state J_x^* as

$$J_x^* = -\frac{(1+C_E)\kappa_i \beta}{\eta}\left(D_v v + D\right) - \bar{J}_W^*(1-\beta) S_{fc} D_v \tag{4.26}$$

The second-order necessary condition for a minimum is

$$\frac{\partial^2 H}{\partial v^2} = \frac{(1+C_E)\kappa_i \beta}{\eta}\left(D_{vv} v + 2D_v\right) + \bar{J}_W^*(1-\beta) S_{fc} D_{vv} \geq 0 \tag{4.27}$$

where D_{vv} is the second-order partial derivative of the drag D with respect to the airspeed v. Using the drag model (2.7), one can write

$$D_v = \rho S C_{D,0} v - \frac{4 C_{D,2} W^2}{\rho S v^3} \tag{4.28}$$

$$D_{vv} = \rho S C_{D,0} + \frac{12 C_{D,2} W^2}{\rho S v^4} \tag{4.29}$$

$$D_W = \frac{4 C_{D,2} W}{\rho S v^2} \tag{4.30}$$

From (4.29), one can conclude that $D_{vv} > 0$, which means that the drag function is strictly convex on the variable v.

From (2.49) and since the Hamiltonian does not depend explicitly on time, one can write

$$\dot{H} = \frac{\partial H}{\partial t} = 0 \tag{4.31}$$

and hence, using (4.17)

$$H(t) = H(t_f) = 0, \ \forall t \in [0, t_f] \tag{4.32}$$

Substituting (2.7), (4.24), (4.26), and (4.28) into the Hamiltonian (4.14) and using (4.32),

one obtains the sextic equation (4.9). A candidate for the solution of the optimal control problem in (4.8) must be a strictly positive real root of (4.9). □

4.2.3 Simulations Results

4.2.3.1 Shooting Method

Based on (4.8), (4.10), (4.11), and (4.19), one obtains the augmented system

$$\begin{aligned}
&\dot{x} = v + v_w \\
&\dot{Q} = -\frac{\beta D v}{\eta U} \\
&\dot{W} = -(1-\beta) S_{fc} D \\
&\dot{J}^*_W = -\frac{4(1+C_E)\kappa_i \beta C_{D,2} W}{\eta \rho S v} - \bar{J}^*_W (1-\beta) S_{fc} \frac{4 C_{D,2} W}{\rho S v^2} \\
&x(0) = x_0,\ x(t_f) = x_f \\
&Q(0) = Q_0,\ W(0) = W_0 \\
&J^*_W(t_f) = 0 \\
&v > 0
\end{aligned} \tag{4.33}$$

The objective of the shooting method is to find an initial condition $J^*_W(0)$ for a trajectory which satisfies the final condition (4.19). Algorithm 3 describes the shooting method used in this section.

Algorithm 3 Shooting Method

1. **Starting Point**:
   (a) Provide an initial guess for $J_W^*(0)$.
   (b) Initialize the parameter $k = 0$.
   (c) Define a tolerance tol, a maximum number of iterations k_{max}, and step size b.
2. **Loop**:
   (a) Simulate (4.33) using a numerical method for ordinary differential equations where the airspeed v is obtained using (4.9) and a root-finding method. Only the strictly positive real root of (4.9) is chosen.
   (b) Compute $\epsilon = {J_W^*}^{[k]}(t_f) - J_W^*(t_f)$.
   (c) Update ${J_W^*}^{[k+1]} = {J_W^*}^{[k]} - b\epsilon$.
   (d) Update $k = k + 1$.
3. **Stopping Criterion**: Stop if $|\epsilon| < tol$ or $k \geq k_{max}$.

This algorithm will be applied to the case of a small unmanned aircraft in different constant wind scenarios. For the simulations, the shooting method parameters are chosen to be

$$\begin{aligned} tol &= 10^{-18} \\ k_{max} &= 10 \\ b &= 1 \end{aligned} \tag{4.34}$$

4.2.3.2 Summary of Results

The simulation results are summarized in Table 4.1. They are obtained based on the augmented system (4.33) and on Theorem 4. The shooting method of Algorithm 3 is used for the simulations.

Table 4.1: Simulation results summary

Experiment	**Results**
v^* as a function of wind speed	Figure 4.1
Energy consumption and DOC as a function of wind speed	Figure 4.2
Pareto-optimal trade-off curve	Figure 4.3

4.2.3.3 Effects of Different Wind Speeds

The model of NASA's GL-10 Greased Lightning hybrid-electric aircraft will be used in the simulations. The aircraft model parameters are presented in Table 3.2. In the simulations, a positive wind speed indicates a tailwind and a negative wind speed indicates a headwind. The simulations are performed for fixed cost coefficients and are listed in Table 3.5. The wind speeds used in the simulations range from -15 m/s to 15 m/s which corresponds to near gale speeds per the Beaufort wind scale [95].

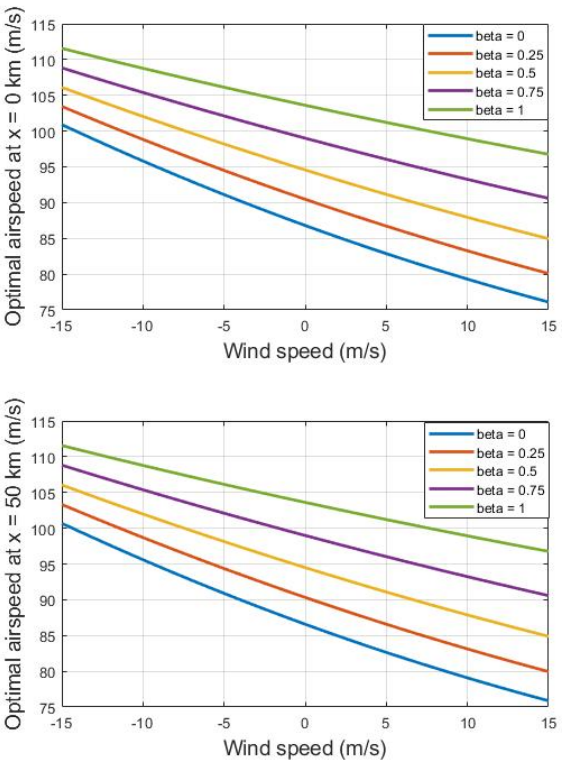

Figure 4.1: Optimal cruise airspeed $v^*(t_0)$ and $v^*(t_f)$ as a function of wind speed when $\beta = 0$, $\beta = 0.25$, $\beta = 0.5$, $\beta = 0.75$, and $\beta = 1$.

In Figure 4.1, one can see that as the wind speed increases, the optimal cruise airspeed decreases. Since a negative wind speed corresponds to a headwind, a negative wind speed means that the aircraft is flying against the wind. Therefore, the aircraft will need a greater airspeed to compensate and minimize the flight duration. Conversely, a positive wind speed

corresponds to a tailwind which means that the aircraft's flight is aided by the wind. Therefore, the aircraft does not need to fly as fast. Since the dynamics of the electric charge (4.5) and the weight (4.4) are not dependent on the wind speed, one should expect that, since the airspeed decreases as the wind speed increases, then the electricity and fuel consumption should also decrease as the wind speed increases. This is verified by Figure 4.2 below. One can see that, indeed, as the wind speed increases, the energy consumption decreases. However, two exceptions to this trend are observed. At $\beta = 0$, no charge is consumed which is consistent with the dynamic equation for the electric charge (4.5). Similarly, at $\beta = 1$, no fuel is consumed which is consistent with the fuel flow rate model (4.4). Additionally, since the DOC (3.6) is dependent on the electricity and fuel consumption, one should expect that the DOC decreases as the wind speed increases which is observed in Figure 4.2.

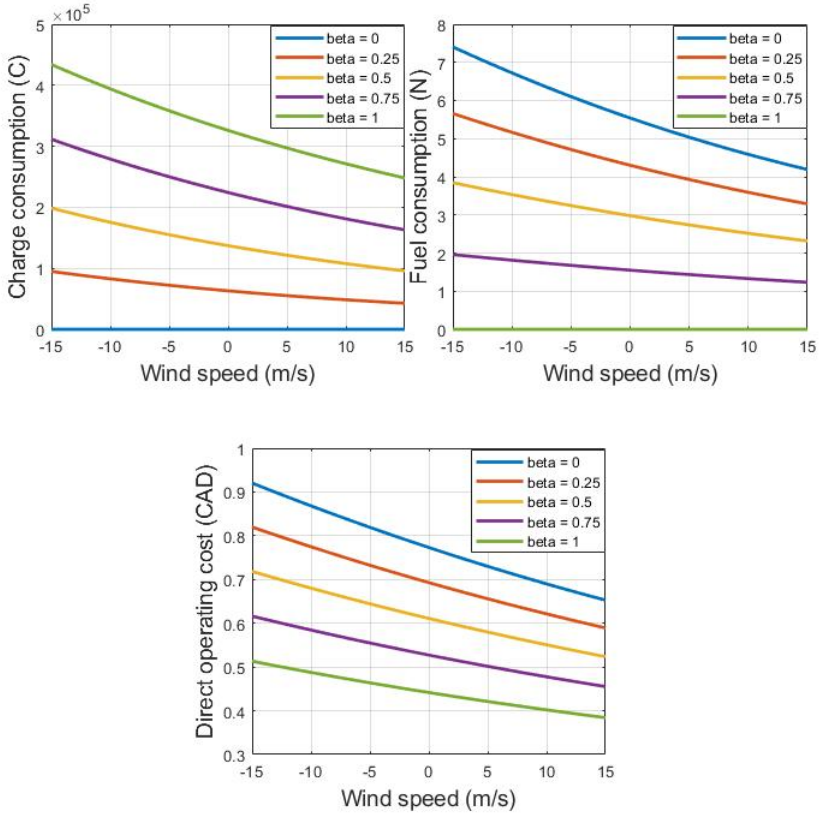

Figure 4.2: Charge and fuel consumed, and direct operating cost as a function of wind speed when $\beta = 0$, $\beta = 0.25$, $\beta = 0.5$, $\beta = 0.75$, and $\beta = 1$.

For $\beta = 0.5$, and simulating the system (4.33) for C_I ranging from 0 to 0.01, one can compute the Pareto-optimal trade-off curves shown in Figure 4.3. The Pareto-optimal trade-off curves for a constant headwind and for a constant tailwind are compared to the no wind scenario which was discussed in Chapter 3. Studying the graphs of Figure 4.2, one should expect that a major difference between the Pareto curves of the three wind scenarios is a shift in the energy consumption. The headwind scenario should lead to the highest energy consumption while the tailwind scenario should lead to the lowest energy consumption.

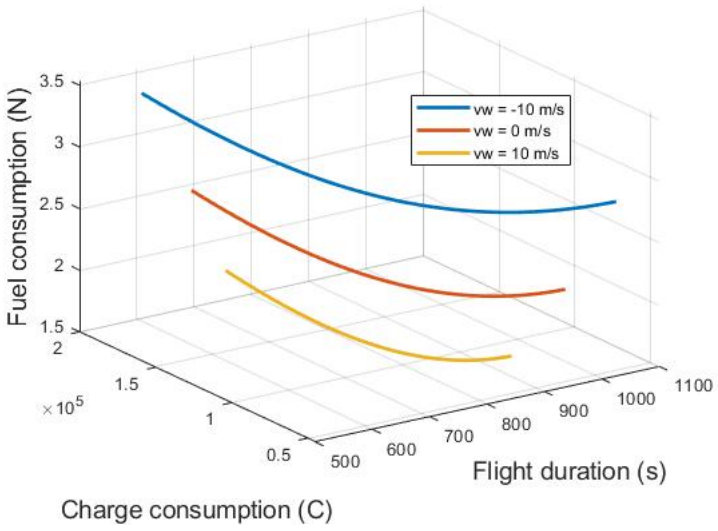

Figure 4.3: Pareto-optimal trade-off curves of NASA GL-10 aircraft in constant wind

From Figure 4.3, one can see that the intuition based on Figure 4.2 discussed previously is verified. One can observe that the main difference between the three scenarios is the energy consumption where the headwind scenario leads to higher energy consumption while the tailwind scenario leads to lower energy consumption.

4.2.3.4 Conclusions

From the simulations presented above, one can draw the following conclusions:

- As the headwind speed increases, the optimal cruise airspeed increases and as the tailwind speed increases, the optimal airspeed decreases. This is shown in Figure 4.1.

- As the headwind speed increases, the electricity and fuel consumption increases and as the tailwind speed increases, the electricity and fuel consumption decreases. This is shown in Figure 4.2 and the Pareto-optimal curves of Figure 4.3.

- As the headwind speed increases, the direct operating cost increases and as the tailwind speed increases, the direct operating cost decreases. This is shown in Figure 4.2.

4.3 Optimal DOC In the Horizontal Plane

4.3.1 Problem Statement

The dynamic model of the hybrid-electric aircraft in this section is based on the flight dynamics in the horizontal plane (2.29)-(2.33) presented in Chapter 2. The propulsion model is based on the fuel consumption model given by (2.35) and (2.36), and the electricity consumption model given by (2.39).

The dynamic model of the hybrid-electric aircraft can be simplified by following the Assumptions 2 to 11 found in the Problem Statement section of Chapter 3 and by assuming that the aircraft heading remains constant. Under these assumptions, the simplified dynamic model of the hybrid-electric aircraft is

$$\dot{x} = v\cos\psi \tag{4.35}$$

$$\dot{y} = v\sin\psi \tag{4.36}$$

$$T = D \tag{4.37}$$

$$L = W \tag{4.38}$$

$$\dot{W} = -(1-\beta)S_{fc}D \tag{4.39}$$

$$\dot{Q} = -\frac{\beta D v}{\eta U} \tag{4.40}$$

where the drag force D is defined in (2.7).

4.3.2 Problem Formulation and Solution

The direct operating cost (DOC) is defined in Chapter 3 (3.6) and minimizing the DOC is equivalent to minimizing the objective functional (3.9) by defining two coefficients (4.6) and (4.7) given that the average of the electricity cost coefficient C_i and the fuel cost coefficient C_f is positive.

Therefore, the optimal control problem based on (4.35)-(4.40), (2.7), and (3.9) can be formulated as

$$\begin{aligned} J^*(x_0) = &\min_{v,t_f} \int_0^{t_f} (C_I + (1+C_E)\kappa_i U i + (1-C_E)\kappa_f f)dt \\ &s.t. \\ &\dot{x} = v\cos\psi \\ &\dot{y} = v\sin\psi \\ &\dot{W} = -(1-\beta)S_{fc}D = -f \\ &\dot{Q} = -\frac{\beta D v}{\eta U} = -i \\ &x(0) = 0,\ x(t_f) = x_f,\ y(0) = 0,\ y(t_f) = y_f \\ &W(0) = W_0,\ Q(0) = Q_0 \end{aligned} \tag{4.41}$$

Theorem 5. *The optimal solution of the optimal control problem (4.41) v^* is a positive real root of the quintic equation*

$$\begin{aligned} &\frac{(1+C_E)\kappa_i\beta\rho^2 S^2 C_{D,0}}{\eta}{v^*}^5 + \frac{\bar{J}_W^*(1-\beta)S_{fc}\rho^2 S^2 C_{D,0}}{2}{v^*}^4 - C_I\rho S{v^*}^2 \\ &- \frac{4(1+C_E)\kappa_i\beta C_{D,2}W^2}{\eta}v^* - 6\bar{J}_W^*(1-\beta)S_{fc}C_{D,2}W^2 = 0 \end{aligned} \tag{4.42}$$

where

$$\bar{J}_W^* = (1-C_E)\kappa_f - J_W^* \tag{4.43}$$

and the time derivative of J_W^* is given by

$$\dot{J}_W^* = -\frac{4(1+C_E)\kappa_i \beta C_{D,2} W}{\eta \rho S v^*} - \bar{J}_W^*(1-\beta) S_{fc} \frac{4 C_{D,2} W}{\rho S v^{*2}} \tag{4.44}$$

with final condition

$$J_W^*(t_f) = 0 \tag{4.45}$$

Proof. One can formulate the Hamiltonian of the optimal control problem (4.41) as

$$H = C_I + (1+C_E)\kappa_i U i + (1-C_E)\kappa_f f + J_x^* \dot{x} + J_y^* \dot{y} + J_W^* \dot{W} + J_Q^* \dot{Q} \tag{4.46}$$

where J_x^*, J_y^*, J_W^*, and J_Q^* are the partial derivatives of the optimal cost-to-go with respect to the latitudinal position x, the longitudinal position y, the weight W, and the electric charge Q.

From the state equations (4.35), (4.36), (4.39), and (4.40), one can rewrite (4.46) as

$$H = C_I + \bar{J}_Q^* \frac{\beta D v}{\eta U} + \bar{J}_W^*(1-\beta) S_{fc} D + J_x^* v \cos\psi + J_y^* v \sin\psi \tag{4.47}$$

where

$$\bar{J}_Q^* = (1+C_E)\kappa_i U - J_Q^* \tag{4.48}$$

and $\bar{J}_W^*$ is defined in (4.43). One can write the vector of terminal conditions $\mathbf{\Psi}$ as

$$\mathbf{\Psi} = \begin{bmatrix} x(t_f) - x_f \\ y(t_f) - y_f \end{bmatrix} = \begin{bmatrix} 0 \\ 0 \end{bmatrix} \tag{4.49}$$

The transversality conditions are then

$$H(t_f) = 0 \tag{4.50}$$

$$J_Q^*(t_f) = \nu \frac{\partial \mathbf{\Psi}}{\partial Q}\bigg|_{t_f} = 0 \tag{4.51}$$

$$J_W^*(t_f) = \nu \frac{\partial \mathbf{\Psi}}{\partial W}\bigg|_{t_f} = 0 \tag{4.52}$$

where ν is a Lagrange multiplier.

The Hamilton's equations for the co-states are

$$\dot{J}_x^* = -\frac{\partial H}{\partial x} = 0 \tag{4.53}$$

$$\dot{J}_y^* = -\frac{\partial H}{\partial y} = 0 \tag{4.54}$$

$$\dot{J}_Q^* = -\frac{\partial H}{\partial Q} = 0 \tag{4.55}$$

$$\dot{J}_W^* = -\frac{\partial H}{\partial W} = -\bar{J}_Q^* \frac{\beta D_W v}{\eta U} - \bar{J}_W^*(1-\beta) S_{fc} D_W \tag{4.56}$$

where D_W is the partial derivative of the drag force with respect to the weight W. From (4.53), (4.54), and (4.55), one can observe that the co-states J_x^*, J_y^*, and J_Q^* are constant. Therefore, the co-state J_Q^* is equal to its final condition (4.51),

$$J_Q^*(t) = 0, \ \forall t \ \in \ [0, t_f] \tag{4.57}$$

Replacing (4.57) into (4.48), one can write

$$\bar{J}_Q^* = (1 + C_E)\kappa_i U \tag{4.58}$$

From (4.47) and Pontryagin's minimum principle, the first-order necessary condition for a

minimum is

$$\frac{\partial H}{\partial v} = \bar{J}_Q^* \frac{\beta(D_v v + D)}{\eta U} + \bar{J}_W^*(1-\beta)S_{fc}D_v + J_x^* \cos\psi + J_y^* \sin\psi = 0 \tag{4.59}$$

where D_v is the partial derivative of the drag D with respect to the airspeed v. Based on (4.58) and on the necessary condition (4.59), one can derive an expression for the co-state J_x^* as

$$J_x^* \cos\psi = -\frac{\beta(1+C_E)\kappa_i}{\eta}(D_v v + D) - \bar{J}_W^* S_{fc}(1-\beta)D_v - J_y^* \sin\psi \tag{4.60}$$

The second-order necessary condition for a minimum is

$$\frac{\partial^2 H}{\partial v^2} = (1+C_E)\kappa_i \beta \left(\frac{D_{vv}v + 2D_v}{\eta}\right) + \bar{J}_W^*(1-\beta)S_{fc}D_{vv} \geq 0 \tag{4.61}$$

where D_{vv} is the second-order partial derivative of the drag D with respect to the airspeed v.

Using the drag model (2.7), one can write

$$D_v = \rho S C_{D,0} v - \frac{4C_{D,2}W^2}{\rho S v^3} \tag{4.62}$$

$$D_{vv} = \rho S C_{D,0} + \frac{12C_{D,2}W^2}{\rho S v^4} \tag{4.63}$$

$$D_W = \frac{4C_{D,2}W}{\rho S v^2} \tag{4.64}$$

From (4.63), one can conclude that $D_{vv} > 0$, which means that the drag function is strictly convex on the variable v.

From (2.49) and since the Hamiltonian does not depend explicitly on time, one can write

$$\dot{H} = \frac{\partial H}{\partial t} = 0 \tag{4.65}$$

and hence, using (4.50)

$$H(t) = H(t_f) = 0, \ \forall t \ \in \ [0, t_f] \tag{4.66}$$

Substituting (2.7), (4.58), (4.60), and (4.62) into the Hamiltonian (4.47) and using (4.66), one obtains the quintic equation (4.42) which is the same expression as in Theorem 3. □

4.3.3 Simulation Results

4.3.3.1 Shooting Method

Based on (4.41), (4.43), (4.44), and (4.52), one constructs the augmented system

$$\begin{aligned}
&\dot{x} = v\cos\psi \\
&\dot{y} = v\sin\psi \\
&\dot{Q} = -\frac{\beta D v}{\eta U} \\
&\dot{W} = -(1-\beta)S_{fc}D \\
&\dot{J}^*_W = -\frac{4(1+C_E)\kappa_i \beta C_{D,2} W}{\eta \rho S v} - \bar{J}^*_W (1-\beta) S_{fc} \frac{4 C_{D,2} W}{\rho S v^2} \\
&x(0) = x_0, \ x(t_f) = x_f, \ y(0) = y_0, \ y(t_f) = y_f \\
&Q(0) = Q_0, \ W(0) = W_0 \\
&J^*_W(t_f) = 0 \\
&v > 0
\end{aligned} \tag{4.67}$$

The objective of the shooting method is to find an initial condition $J^*_W(0)$ for a trajectory which satisfies the final condition (4.52). Algorithm 4 describes the shooting method. This algorithm will be applied to the case of a small unmanned aircraft.

Algorithm 4 Shooting Method

1. **Starting Point**:
   (a) Provide an initial guess for $J_W^*(0)$.
   (b) Initialize the parameter $k = 0$.
   (c) Define a tolerance tol, a maximum number of iterations k_{max}, and a step size b.
2. **Loop**:
   (a) Simulate (4.67) using a numerical method for ordinary differential equations where the airspeed v is obtained using (4.42) and a root-finding method. Only the strictly positive real root of (4.42) is chosen.
   (b) Compute $\epsilon = {J_W^*}^{[k]}(t_f) - J_W^*(t_f)$.
   (c) Update ${J_W^*}^{[k+1]}(t_f) = {J_W^*}^{[k]}(t_f) - b\epsilon$.
   (d) Update $k = k + 1$.
3. **Stopping Criterion**: Stop if $|\epsilon| < tol$ or $k \geq k_{max}$

The parameters of Algorithm 4 used for the simulations are as follows

$$\begin{aligned} tol &= 10^{-18} \\ k_{max} &= 10 \\ b &= 1 \end{aligned} \tag{4.68}$$

4.3.3.2 Effects of Different C_E

The aircraft model used in the following simulations is that of NASA's GL-10 Greased Lightning hybrid-electric aircraft. Its parameters are listed in Table 3.2.

The simulation parameters to examine the effects of different values of C_E on the aircraft trajectory are listed in Table 4.2. The total distance traveled is selected to be 50 km which corresponds to the distance between the easternmost and westernmost points of Montréal Island in Québec, Canada as shown in Figure 3.2.

Table 4.2: Simulation parameters

Parameter	Value
Air density (100 m)	1.225 kg/m^3
Initial latitudinal position x_0	0 km
Final latitudinal position x_f	36.65 km
Initial longitudinal position y_0	0 km
Final longitudinal position y_f	34 km
Initial charge Q_0	62,496 C
Initial weight W_0	275 N
Heading angle ψ	42.86°
Hybridization coefficient β	0.5

Using the aircraft parameters of Table 3.2 and the simulation parameters of Table 4.2, one can produce aircraft trajectories for different values of C_E.

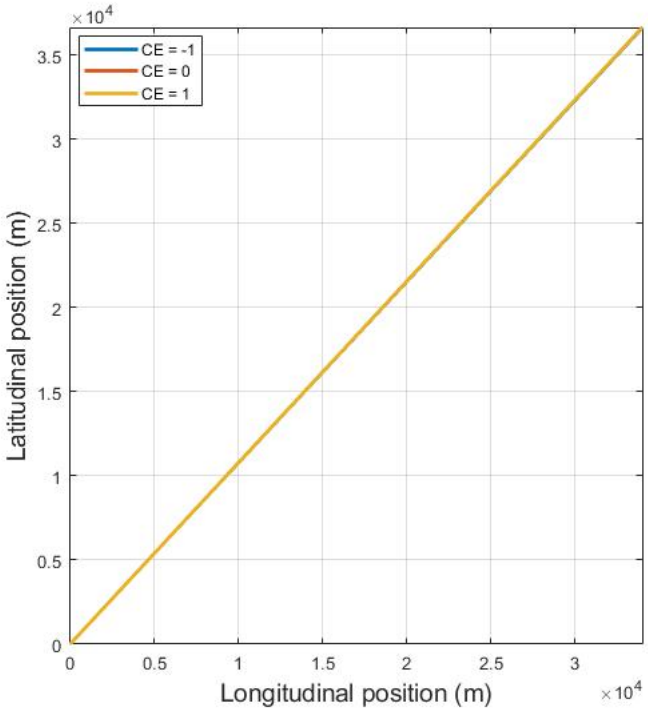

Figure 4.4: Aircraft trajectory in two-dimensional space at $C_I = 0$ when $C_E = -1$, $C_E = 0$, and $C_E = 1$.

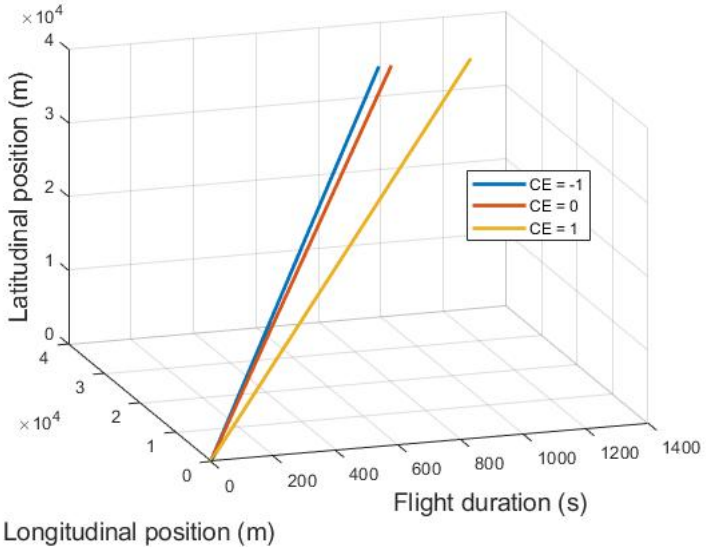

Figure 4.5: Aircraft trajectory with respect to time at $C_I = 0$ when $C_E = -1$, $C_E = 0$, and $C_E = 1$.

In Figure 4.4, one can observe that the aircraft trajectories in two-dimensional space for the three C_E scenarios are linear. One can expect such a result as the heading angle was defined as a constant. Furthermore, in Figure 4.5, the aircraft trajectories for the three different C_E with respect to the flight duration is nonlinear, but close to linear. Such a phenomenon is expected in the case where $\beta \neq 1$. As fuel is consumed, the aircraft becomes lighter and its optimal airspeed changes consequently. As a result, the relationship between the aircraft trajectories and time is nonlinear. However, if $\beta = 1$, then no fuel is consumed and the relationship should be linear.

Chapter 5

Conclusions and Future Work

To help transition to zero-emissions aviation and to meet the demands in optimal flight and energy management for efficient advanced air mobility, this thesis addressed three problems of optimal flight management and energy management of hybrid-electric aircraft based on the direct operating cost of the aircraft.

The first problem was the minimization of the direct operating cost (DOC) of a hybrid-electric aircraft in steady cruise flight without wind. In this problem, only the longitudinal flight dynamics were considered. To solve this problem, an energy management parameter, called the hybridization coefficient in this thesis, was first defined as the proportion of the total thrust of the hybrid-electric aircraft which comes from electrical energy. A quintic polynomial whose positive real roots are solutions to the minimum DOC problem was then found using Pontryagin's Minimum Principle (PMP).

The effects of varying the ratio between the time-related costs and the energy costs C_I was investigated and we concluded that as the time-related costs increased relative to the energy costs, the aircraft flew faster (see Figures 3.3 and 3.6). Furthermore, the investigation found that when the fuel cost is very large compared to the electricity cost, the optimal airspeed of the aircraft approached the solution of the all-fuel aircraft presented in [5] while a large electricity cost relative to fuel cost led the optimal solution to approach that of the all-electric

aircraft in [3] (see Figure 3.3). In fact, from the definition of the direct operating cost (3.6), one can see that, if the electricity cost $C_i = 0$, only the fuel and time components remain in the DOC and, if the fuel cost $C_f = 0$, only the electricity and time components remain in the DOC, which correspond to the all-fuel and all-electric formulation of the DOC, respectively. Additionally, a greater C_I led to greater fuel and electricity consumption (see Figures 3.4 and 3.7). Then, examining the effects of varying the energy management parameter led to an interesting finding. The results suggested that an optimal energy management strategy to minimize the DOC for hybrid-electric aircraft is either to use only fuel or only electrical energy which was validated through multiple scenarios (see Figures 3.5 and 3.8). Finally, a case study of hydrogen hybrid-electric aircraft was performed where it was found that, the hydrogen aircraft can lead to lower direct operating cost than the kerosene-fuel aircraft (see Figure 3.9).

The second problem extended the first problem to account for constant wind. A sextic polynomial whose positive real roots are solutions of the minimum DOC problem was found using PMP. An investigation of the aircraft airspeed under different wind speeds showed that, as the tailwind speed increased, the optimal airspeed decreased and, conversely, as the headwind speed increased, the optimal airspeed increased (see Figure 4.1). Furthermore, a greater headwind led to more energy consumption while a greater tailwind led to lower energy consumption (see Figure 4.2). Similarly, a greater headwind increased the DOC while a greater tailwind decreased the DOC (see Figure 4.2).

Finally, the third problem was an extension of the first problem to the steady cruise flight in the horizontal plane. The problem is defined for a weak wind and constant heading scenario. A quintic polynomial whose positive real roots are solutions to this problem was obtained using PMP with simulations supporting the solutions (see Figures 4.4 and 4.5).

To summarize, the main contributions of this thesis are the solutions of the optimal airspeed which minimizes the direct operating cost of a hybrid-electric aircraft in steady cruise flight subject to wind and in the horizontal plane not subject to wind, a case study of

hydrogen hybrid-electric aircraft using the solutions found for the minimum direct operating cost, and the investigation of a possible optimal energy management strategy based on the hybridization coefficient. The key results from the simulations showed that in Figures 3.3 and 3.6, as C_I increased, the optimal airspeed increased. Then, from Table 3.6, an optimal energy management strategy for the hybrid-electric aircraft seems to be either to use only fuel or only electrical energy. Furthermore, from Figures 4.1 and 4.2, as the tailwind speed increased, the optimal airspeed, the DOC, and the energy consumption decreased. Conversely, as the headwind speed increased, the optimal airspeed, the DOC, and the energy consumption increased. Finally, from Figure 3.9, hydrogen hybrid-electric aircraft seems to lead to lower direct operating costs than kerosene-fuel hybrid-electric aircraft.

5.1 Future Work

The work presented in this thesis may be extended along the following avenues:

- Formal proof of the optimal energy management strategy based on the hybridization coefficient.
- Optimal DOC for the climb and descent phases of the hybrid-electric aircraft.
- Optimal DOC with lateral winds and time-varying wind fields.
- Optimal DOC for the hybrid-electric aircraft flight in three-dimensional space.
- Incorporating a battery charging model for the hybrid-electric aircraft.
- Implementation of the solutions in this thesis for optimal trajectory planning of hybrid-electric aircraft.
- Development of optimal control laws based on the set-point solutions proposed in this thesis.

Bibliography

[1] H. Ritchie and M. Roser, "Urbanization," June 2018. [Online]. Available: https://ourworldindata.org/urbanization

[2] SKYbrary, "Antonov an-225 mriya," December 2014. [Online]. Available: https://www.skybrary.aero/index.php/A225

[3] M. Kaptsov and L. Rodrigues, "Electric aircraft flight management systems: Economy mode and maximum endurance," *Journal of Guidance, Control, and Dynamics*, vol. 41, no. 1, pp. 288–293, 2018.

[4] G. Maps, "Montreal island." [Online]. Available: http://www.google.ca/maps/@45.5149034,-73.7373231,10.92z/data=!5m1!1e4

[5] J. Villarroel and L. Rodrigues, "Optimal control framework for cruise economy mode of flight management systems," *Journal of Guidance, Control, and Dynamics*, vol. 39, no. 5, pp. 1022–1033, 2016.

[6] "World urbanization prospects - population division." [Online]. Available: https://population.un.org/wup/

[7] O. Wright, "Telegram from orville wright in kitty hawk, north carolina, to his father announcing four successful flights, 1903 december 17," Dec 1903. [Online]. Available: https://www.wdl.org/en/item/11372/

[8] "Nasa's ingenuity mars helicopter succeeds in historic first flight – nasa's mars exploration program," Apr 2021. [Online]. Available: https://mars.nasa.gov/news/8923/nasas-ingenuity-mars-helicopter-succeeds-in-historic-first-flight/

[9] D. L. Hackenberg, "Nasa advanced air mobility (aam) urban air mobility (uam) and grand challenge aiaa," 2019.

[10] E. M. Johnson, "Boeing says its fleet will be able to fly on 100% biofuel by 2030," Jan 2021. [Online]. Available: https://www.reuters.com/article/us-boeing-biofuels-idUSKBN29R2C4

[11] J. Köhler, R. Walz, F. Marscheder-Weidemann, and B. Thedieck, "Lead markets in 2nd generation biofuels for aviation: A comparison of germany, brazil and the usa," *Environmental Innovation and Societal Transitions*, vol. 10, pp. 59–76, 2014.

[12] Airbus, "Airbus reveals new zero-emission concept aircraft," Sep 2020. [Online]. Available: https://www.airbus.com/newsroom/press-releases/en/2020/09/airbus-reveals-new-zeroemission-concept-aircraft.html

[13] G. D. Brewer, *Hydrogen aircraft technology*. Routledge, 2017.

[14] P. Wheeler, "Technology for the more and all electric aircraft of the future," in *2016 IEEE International Conference on Automatica (ICA-ACCA)*. IEEE, 2016, pp. 1–5.

[15] J. Van Bogaert, "Assessment of potential fuel saving benefits of hybrid-electric regional aircraft," 2015.

[16] M. Voskuijl, J. Van Bogaert, and A. G. Rao, "Analysis and design of hybrid electric regional turboprop aircraft," *CEAS Aeronautical Journal*, vol. 9, no. 1, pp. 15–25, 2018.

[17] C. Silva, W. R. Johnson, E. Solis, M. D. Patterson, and K. R. Antcliff, "Vtol urban air mobility concept vehicles for technology development," in *2018 Aviation Technology, Integration, and Operations Conference*, 2018, p. 3847.

[18] D. D. Currin, "Air force soil stabilization research," Air Force Weapons Lab Kirtland AFB NM Civil Engineering Div, Tech. Rep., 1970.

[19] W. D. Collier, "Afwl technical objective number 3: Civil engineering rdt and e," Air Force Weapons Lab Kirtland AFB NM, Tech. Rep., 1973.

[20] D. J. Wing, E. T. Chancey, M. S. Politowicz, and M. G. Ballin, "Achieving resilient in-flight performance for advanced air mobility through simplified vehicle operations," in *AIAA Aviation 2020 Forum*, 2020, p. 2915.

[21] E. T. Chancey and M. S. Politowicz, "Designing and training for appropriate trust in increasingly autonomous advanced air mobility operations: A mental model approach version," 2020.

[22] E. T. Chancey, M. S. Politowicz, and L. Le Vie, "Enabling advanced air mobility operations through appropriate trust in human-autonomy teaming: Foundational research approaches and applications," in *AIAA Scitech 2021 Forum*, 2021, p. 0880.

[23] Í. R. de Oliveira, E. C. P. Neto, T. T. Matsumoto, and H. Yu, "Decentralized air traffic management for advanced air mobility," in *2021 Integrated Communications Navigation and Surveillance Conference (ICNS)*. IEEE, 2021, pp. 1–8.

[24] J. Lundberg, K. L. Palmerius, and B. Josefsson, "Urban air traffic management (utm) implementation in cities-sampled side-effects," in *2018 IEEE/AIAA 37th Digital Avionics Systems Conference (DASC)*. IEEE, 2018, pp. 1–7.

[25] V. Battiste, A.-Q. V. Dao, T. Z. Strybel, A. Boudreau, and Y. K. Wong, "Function allocation strategies for the unmanned aircraft system traffic management (utm) sys-

tem, and their impact on skills and training requirements for utm operators," *IFAC-PapersOnLine*, vol. 49, no. 19, pp. 42–47, 2016.

[26] J. Homola, Q. Dao, L. Martin, J. Mercer, C. Mohlenbrink, and L. Claudatos, "Technical capability level 2 unmanned aircraft system traffic management (utm) flight demonstration: Description and analysis," in *2017 IEEE/AIAA 36th Digital Avionics Systems Conference (DASC)*. IEEE, 2017, pp. 1–10.

[27] B. Li, J. Zhang, L. Dai, K. L. Teo, and S. Wang, "A hybrid offline optimization method for reconfiguration of multi-uav formations," *IEEE Transactions on Aerospace and Electronic Systems*, 2020.

[28] S.-H. Kim, G. E. G. Padilla, K.-J. Kim, and K.-H. Yu, "Flight path planning for a solar powered uav in wind fields using direct collocation," *IEEE Transactions on Aerospace and Electronic Systems*, vol. 56, no. 2, pp. 1094–1105, 2019.

[29] S. He, H.-S. Shin, A. Tsourdos, and C.-H. Lee, "Energy-optimal waypoint-following guidance considering autopilot dynamics," *IEEE Transactions on Aerospace and Electronic Systems*, vol. 56, no. 4, pp. 2701–2717, 2019.

[30] S. M.-B. Malaek and M. Golchoubian, "Enhanced conflict resolution maneuvers for dense airspaces," *IEEE Transactions on Aerospace and Electronic Systems*, vol. 56, no. 5, pp. 3409–3420, 2020.

[31] A. Rodionova, Y. V. Pant, K. Jang, H. Abbas, and R. Mangharam, "Learning-to-fly: Learning-based collision avoidance for scalable urban air mobility," in *2020 IEEE 23rd International Conference on Intelligent Transportation Systems (ITSC)*. IEEE, 2020, pp. 1–8.

[32] ICAO, "Climate change," 2020. [Online]. Available: https://www.icao.int/environmental-protection/pages/climate-change.aspx

[33] ——. (2021) Electric and hybrid aircraft platform for innovation. [Online]. Available: https://www.icao.int/environmental-protection/Pages/electric-aircraft.aspx

[34] M. Harmats and D. Weihs, "Hybrid-propulsion high-altitude long-endurance remotely piloted vehicle," *Journal of Aircraft*, vol. 36, no. 2, pp. 321–331, 1999.

[35] R. Hiserote and F. Harmon, "Analysis of hybrid-electric propulsion system designs for small unmanned aircraft systems," in *8th Annual International Energy Conversion Engineering Conference*, 2010, p. 6687.

[36] H. Chen and A. Khaligh, "Hybrid energy storage system for unmanned aerial vehicle (uav)," in *IECON 2010-36th Annual Conference on IEEE Industrial Electronics Society*. IEEE, 2010, pp. 2851–2856.

[37] A. Gibson, D. Hall, M. Waters, P. Masson, B. Schiltgen, T. Foster, and J. Keith, "The potential and challenge of turboelectric propulsion for subsonic transport aircraft," in *48th AIAA Aerospace Sciences Meeting Including the New Horizons Forum and Aerospace Exposition*, 2010, p. 276.

[38] F. G. Harmon, A. A. Frank, and S. S. Joshi, "The control of a parallel hybrid-electric propulsion system for a small unmanned aerial vehicle using a cmac neural network," *Neural Networks*, vol. 18, no. 5, pp. 772–778, 2005.

[39] F. G. Harmon, A. A. Frank, and J.-J. Chattot, "Conceptual design and simulation of a small hybrid-electric unmanned aerial vehicle," *Journal of Aircraft*, vol. 43, no. 5, pp. 1490–1498, 2006.

[40] C. Pornet, S. Kaiser, and C. Gologan, "Cost-based flight technique optimization for hybrid energy aircraft," *Aircraft Engineering and Aerospace Technology*, vol. 86, no. 6, pp. 591–598, 2014.

[41] R. D. Falck, J. S. Gray, and B. Naylor, "Parallel aircraft trajectory optimization with analytic derivatives," in *17th AIAA/ISSMO Multidisciplinary Analysis and Optimization Conference*, 2016, p. 3207.

[42] E. Bongermino, F. Mastrorocco, M. Tomaselli, V. Monopoli, and D. Naso, "Model and energy management system for a parallel hybrid electric unmanned aerial vehicle," in *2017 IEEE 26th International Symposium on Industrial Electronics (ISIE)*. IEEE, 2017, pp. 1868–1873.

[43] T. Donateo and L. Spedicato, "Fuel economy of hybrid electric flight," *Applied energy*, vol. 206, pp. 723–738, 2017.

[44] L. Boggero, M. Fioriti, C. S. Ragusa, and S. Corpino, "Trade off studies of hybrid-electric aircraft by fuzzy logic methodology," *International Journal of Applied Electromagnetics and Mechanics*, vol. 56, no. S1, pp. 143–152, 2018.

[45] T. Donateo, A. Ficarella, and L. Spedicato, "A method to analyze and optimize hybrid electric architectures applied to unmanned aerial vehicles," *Aircraft Engineering and Aerospace Technology*, 2018.

[46] I. Geiss, S. Notter, A. Strohmayer, and W. Fichter, "Optimized operation strategies for serial hybrid-electric aircraft," in *2018 Aviation Technology, Integration, and Operations Conference*, 2018, p. 4230.

[47] M. Doff-Sotta, M. Cannon, and M. Bacic, "Optimal energy management for hybrid electric aircraft," *arXiv preprint arXiv:2004.02582*, 2020.

[48] J. P. S. P. Leite and M. Voskuijl, "Optimal energy management for hybrid-electric aircraft," *Aircraft Engineering and Aerospace Technology*, 2020.

[49] T. J. Wall and R. T. Meyer, "Hybrid electric aircraft switched model optimal control," *Journal of Propulsion and Power*, vol. 36, no. 4, pp. 488–497, 2020.

[50] W. Wang and J. P. Koeln, "Hierarchical multi-timescale energy management for hybrid-electric aircraft," in *Dynamic Systems and Control Conference*, vol. 84270. American Society of Mechanical Engineers, 2020, p. V001T11A002.

[51] R. de Vries, M. F. Hoogreef, and R. Vos, "Range equation for hybrid-electric aircraft with constant power split," *Journal of Aircraft*, vol. 57, no. 3, pp. 552–557, 2020.

[52] K. Sun, J. Li, H. Liang, and M. Zhu, "Simulation of a hybrid energy system for stratospheric airships," *IEEE Transactions on Aerospace and Electronic Systems*, vol. 56, no. 6, pp. 4426–4436, 2020.

[53] S. R. Hashemi, A. Bahadoran Baghbadorani, R. Esmaeeli, A. Mahajan, and S. Farhad, "Machine learning-based model for lithium-ion batteries in bms of electric/hybrid electric aircraft," *International Journal of Energy Research*, vol. 45, no. 4, pp. 5747–5765, 2021.

[54] M. Wang and M. Mesbahi, "Power allocation for hybrid electric aircraft via optimal control during climb, cruise, and descent," in *AIAA Scitech 2021 Forum*, 2021, p. 0640.

[55] H. Lee, C. M. Harris, J. C. Gladin, and D. N. Mavris, "A method for simultaneous optimization of power split and flight path trajectories for hybrid electric aircraft," in *AIAA Scitech 2021 Forum*, 2021, p. 1010.

[56] A. Dupont, "Liquid hydrogen as a supersonic transport fuel," in *Advances in Cryogenic Engineering: Proceedings of the 1966 Cryogenic Engineering Conference University of Colorado Engineering Research Center and Cryogenics Division NBS Institute for Materials Research Boulder, Colorado June 13–15, 1966*. Springer, 1967, pp. 1–10.

[57] G. Brewer, "Prospects for hydrogen aircraft," *SAE Transactions*, pp. 2309–2320, 1980.

[58] G. D. Brewer, R. E. Morris, R. H. Lange, and J. W. Moore, "Study of the application of hydrogen fuel to long-range subsonic transport aircraft," *NASA CR*, vol. 132559, 1975.

[59] D. G. Victor, "Liquid hydrogen aircraft and the greenhouse effect," *International Journal of Hydrogen Energy*, vol. 15, no. 5, pp. 357–367, 1990.

[60] A. Contreras, S. Yiğit, K. Özay, and T. Veziroğlu, "Hydrogen as aviation fuel: a comparison with hydrocarbon fuels," *International Journal of Hydrogen Energy*, vol. 22, no. 10-11, pp. 1053–1060, 1997.

[61] M. J. Sefain, "Hydrogen aircraft concepts and ground support," 2005.

[62] H. G. Klug and R. Faass, "Cryoplane: hydrogen fuelled aircraft—status and challenges," *Air & Space Europe*, vol. 3, no. 3-4, pp. 252–254, 2001.

[63] G. Corchero and J. Montanes, "An approach to the use of hydrogen for commercial aircraft engines," *Proceedings of the Institution of Mechanical Engineers, Part G: Journal of Aerospace Engineering*, vol. 219, no. 1, pp. 35–44, 2005.

[64] A. Westenberger, "Cryoplane–hydrogen aircraft," *H2 Expo (11 October Hamburg 2003), Available from World Wide Web:¡ http://www. h2hh. de/downloads/Westenberger. pdf*, 2003.

[65] D. Maniaci, "Relative performance of a liquid hydrogen-fueled commercial transport," in *46th AIAA Aerospace sciences meeting and exhibit*, 2008, p. 152.

[66] C. Amy and A. Kunycky, "Hydrogen as a renewable energy carrier for commercial aircraft," *arXiv preprint arXiv:1910.05632*, 2019.

[67] P. Derakhshandeh, A. Ahmadi, and R. Dashti, "Simulation and technical-economic-environmental optimization of the general electric ge90 hydrogen turbofan engine," *International Journal of Hydrogen Energy*, 2020.

[68] S. Boggia and A. Jackson, "Some unconventional aero gas turbines using hydrogen fuel," in *Turbo Expo: Power for Land, Sea, and Air*, vol. 3607, 2002, pp. 683–690.

[69] J. D. Anderson, *Aircraft performance and design.* McGraw-Hill, 1999.

[70] G. G. Slabaugh, "Computing euler angles from a rotation matrix," *Retrieved on August*, vol. 6, no. 2000, pp. 39–63, 1999.

[71] A. Tewari, *Advanced Control of Aircraft, Spacecraft and Rockets.* John Wiley and Sons, 2011.

[72] D. G. Hull *et al.*, *Fundamentals of airplane flight mechanics.* Springer, 2007, vol. 19.

[73] D. Verstraete, "The potential of liquid hydrogen for long range aircraft propulsion," 2009.

[74] L. Das, "Hydrogen-oxygen reaction mechanism and its implication to hydrogen engine combustion," *International Journal of Hydrogen Energy*, vol. 21, no. 8, pp. 703–715, 1996.

[75] T.-S. Wang, "Thermophysics characterization of kerosene combustion," *Journal of Thermophysics and Heat Transfer*, vol. 15, no. 2, pp. 140–147, 2001.

[76] R. Bellman, "Dynamic programming," *Science*, vol. 153, no. 3731, pp. 34–37, 1966.

[77] L. S. Pontryagin, V. G. Boltyanskii, R. V. Gamkrelidze, and E. F. Mishchenko, *The Mathematical Theory of Optimal Processes.* Interscience Publishers, 1962.

[78] J.-B. Hiriat-Urruty, *Les mathématiques du mieux faire - Volume 2: La commande optimale pour les débutants.* ellipses, 2008, vol. 2.

[79] A. Gomes, I. Voiculescu, J. Jorge, B. Wyvill, and C. Galbraith, *Implicit Curves and Surfaces: Mathematics, Data Structures and Algorithms.* Springer-Verlag London, 2009.

[80] M. R. Osborne, "On shooting methods for boundary value problems," *Journal of mathematical analysis and applications*, vol. 27, no. 2, pp. 417–433, 1969.

[81] K. Brown, "2020 tied for warmest year on record, nasa analysis shows," Jan 2021. [Online]. Available: https://www.nasa.gov/press-release/2020-tied-for-warmest-year-on-record-nasa-analysis-shows

[82] "Zeroe." [Online]. Available: https://www.airbus.com/innovation/zero-emission/hydrogen/zeroe.html

[83] "Boeing set to fly with aircraft using sustainable fuels," Jan 2021. [Online]. Available: https://biofuels-news.com/news/boeing-set-to-fly-with-aircraft-using-sustainable-fuels/

[84] "Electric and hybrid aircraft platform for innovation (e-hapi) //." [Online]. Available: https://www.icao.int/environmental-protection/Pages/electric-aircraft.aspx

[85] C. M. Shepherd, "Design of primary and secondary cells: Ii. an equation describing battery discharge," *Journal of the Electrochemical Society*, vol. 112, no. 7, p. 657, 1965.

[86] J. Roskam and C.-T. E. Lan, *Airplane aerodynamics and performance*. DARcorporation, 1997.

[87] T. Donateo, A. Ficarella, L. Spedicato, A. Arista, and M. Ferraro, "A new approach to calculating endurance in electric flight and comparing fuel cells and batteries," *Applied energy*, vol. 187, pp. 807–819, 2017.

[88] P. W. Government of Canada and G. S. Canada, "Government of canada." [Online]. Available: https://canadagazette.gc.ca/rp-pr/p2/2019/2019-01-09/html/sor-dors11-eng.html

[89] Hydro-Québec, "Domestic rates: Hydro-québec," 2021. [Online]. Available: https://www.hydroquebec.com/residential/customer-space/rates/

[90] "Canada gasoline prices1992-2021 data: 2022-2023 forecast: Historical: Chart." [Online]. Available: https://tradingeconomics.com/canada/gasoline-prices

[91] E. De Grave, *Reverse Engineering of Passenger Jets–Classified Design Parameters*. Hamburg: Aircraft Design and Systems Group (AERO), Department of Automotive . . . , 2017.

[92] S. G. A. L. A. RJ100 and S. G. A. Lines, "British aerospace 146 british aerospace 146."

[93] "E-fan x." [Online]. Available: https://www.airbus.com/innovation/zero-emission/electric-flight/e-fan-x.html

[94] "Reported operating cost and utilization of more than 3,000 narrowbody aircraft." [Online]. Available: https://www.planestats.com/bhsn_2014dec

[95] "Government of canada," Mar 2017. [Online]. Available: https://www.canada.ca/en/environment-climate-change/services/general-marine-weather-information/understanding-forecasts/beaufort-wind-scale-table.html